Chemical Engineering Journal 526 (2025) 170755

Contents lists available at ScienceDirect

Chemical Engineering Journal

journal homepage: www.elsevier.com/locate/cej

Enhancing CO_2 hydrogenation to methanol in fixed and fluidized bed reactors by selective in-situ adsorption of water☆

Chiara Berretta [a,b], Mauro Andrea Pappagallo [a,b], Emanuele Moioli [a,c], Oliver Kröcher [a,b], Tilman J. Schildhauer [a,*]

[a] PSI Center for Energy and Environmental Sciences, Paul Scherrer Institut, 5232 Villigen PSI, Switzerland
[b] Institute of Chemical Sciences and Engineering, École Polytechnique Fédérale de Lausanne, 1015 Lausanne, Switzerland
[c] Department of Chemistry, Materials and Chemical Engineering, Politecnico di Milano, 20133 Milano, Italy

ARTICLE INFO

Keywords:
Sorption-enhanced methanol synthesis
Zeolite 3A
Fluidized-bed reactor
Fixed-bed reactor
CO_2 hydrogenation

ABSTRACT

Methanol synthesis offers a significant pathway for carbon dioxide valorization and hydrogen storage. However, carbon dioxide hydrogenation to methanol is thermodynamically limited. To couple the process with biogenic carbon dioxide supply from organic wastes and green hydrogen, a way to shift the equilibrium by other means than the pressure must be found. This work investigates the underlying aspects of sorption-enhanced methanol synthesis by selective steam removal in fixed and bubbling fluidized bed configurations. Zeolite 3 A is chosen as a suitable sorbent based on its selectivity towards water and retention of sorption capacity between 220 and 280 °C. A dynamic model for simulation of the fixed-bed sorption-enhanced methanol synthesis shows reactor performance at the targeted application pressure of 20–30 bar. Enhanced product yields beyond thermodynamic equilibrium limits are obtained in a lab-scale reactor at 3 bar and 220–250 °C via over-stochiometric water adsorption. In both reactor configurations, low-pressure enhancement primarily promotes carbon monoxide yield. Predicted methanol yields at higher pressures reach similar values, which suggests implementing a two-stage process. The additional production relative to the total output expected under full equilibrium limitation results in a 14–23 % integrated enhancement for methanol and 17–20 % for carbon monoxide, depending on temperature and reactor configuration. During the sorption-enhancement peak, the maximum achievable yields reach 130–175 % and 160–185 %, respectively. The transient nature of sorption enhancement is highlighted, suggesting a fluidized reactor design for continuous regeneration in a separate vessel, promoted by a sharper water breakthrough than in a fixed bed, a more compact reactor volume, and improved temperature distribution.

Nomenclature

A	reactor cross-sectional area	m^2
b_{H_2O}	Langmuir adsorption isotherm parameter	Pa^{-1}
$b^0_{H_2O}$	preexponential factor for Langmuir adsorption isotherm parameter	Pa^{-1}
D_t	reactor tube diameter	m
$\mathscr{D}_c$	micropore diffusivity	$\frac{m^2}{s}$
F_i	component i molar flow rate	$\frac{kmol}{s}$
k_a	mass transport constant for adsorption model	$\frac{1}{s}$

(*continued on next column*)

(*continued*)

k_j	rate constant for the reaction j	$\frac{kmol}{kg \bullet s \bullet bar^n}$
K_j^{eq}	equilibrium constant for for the reaction j	bar^{-n}
K_i	adsorption constant of the species i on the catalyst surface	bar^{-n}
m_{H_2O}	sorbent saturation capacity	$\frac{kmol}{kg}$
m_i	mass of component i	kg
P_i	partial pressure of component i	Pa or bar
q	water adsorption loading	$\frac{kmol}{kg}$
q^*	equilibrium water adsorption loading	$\frac{kmol}{kg}$

(*continued on next page*)

☆ This article is part of a Special issue entitled: 'ISCRE 28' published in Chemical Engineering Journal.

* Corresponding author.
E-mail address: tilman.schildhauer@psi.ch (T.J. Schildhauer).

https://doi.org/10.1016/j.cej.2025.170755
Received 8 December 2024; Received in revised form 21 August 2025; Accepted 10 November 2025
Available online 12 November 2025

(*continued*)

R	universal gas constant	$\frac{J}{K \bullet mol}$
r_c	micropore radius	m
r_j	reaction rate of reaction j	$\frac{kmol}{kg \bullet s}$
T	temperature	K
t	time	s
t_{et}	empty tube residence time	s
$\langle t \rangle$	average residence time	s
v_{et}	empty tube velocity	$\frac{m}{s}$
v_G	gas velocity	$\frac{m}{s}$
Y_i	yield of component i	%
z	axial coordinate along the reactor	m
ΔH_r^0	standard enthalpy change for the reaction	$\frac{kJ}{mol}$
$\Delta h_{H_2O}^{ads}$	adsorption heat of water on sorbent	$\frac{J}{mol}$
α	fitting parameter	–
ε	overall void fraction	–
φ	sorbent volume fraction over all solid	–
ν_{ij}	stoichiometric coefficient of species i in reaction j	–
ρ_A	sorbent density	$\frac{kg}{m^3}$
ρ_C	catalyst density	$\frac{kg}{m^3}$
ηSE	sorption-enhancement contribution	wt.-%

List of acronyms

BFB	Bubbling Fluidized Bed
CZA	Copper/Zinc Oxide/Aluminum Oxide
FB	Fixed Bed
GHSV	Gas Hourly Space Velocity
HP	High-Pressure
LDF	Linear Driving Force
LP	Low-Pressure
MFC	Mass Flow Controller
MS	Mass Spectrometer
m/z	Mass-to-charge ratio
NDIR	Non-Dispersive Infrared
ODE	Ordinary Differential Equation
PSA	Pressure Swing Adsorption
PSD	Particle Size Distribution
PtX	Power-to-X
RMSE	Root Mean Squared Error
RWGS	Reverse Water Gas Shift Reaction
SC	Standard Conversion
SE	Sorption-Enhanced
TRL	Technology Readiness Level

1. Introduction

In a world where the concern for increasing carbon dioxide (CO_2) levels is fostering new industrial processes, methanol (CH_3OH or MeOH) could be a key chemical for the upcycling of CO_2. Methanol already represents a key product in the industrial sector, as it is the feedstock to produce several chemicals, including dimethyl ether (DME), methyl-tert-butyl ether, acetic acid, and formaldehyde [1]. As a chemical energy carrier, methanol can be used directly as a fuel, for example in direct methanol fuel cells, where its chemical energy is converted into electrical power under ambient pressure conditions [2]. Alternatively, it can be blended with gasoline and diesel to replace fossil fuels in internal combustion engines [3]. The potential of methanol extends further as a hydrogen (H_2) storage molecule, positioning methanol derived from captured or biogenic CO_2 combined with green hydrogen as a highly promising fuel for the energy transition, particularly in the mobility [4], and aviation [5] sectors. Notably, in the existing industrial processes, significant amounts of CO_2 are already added to the syngas feedstock for methanol production [6], confirming the potential of methanol for converting waste CO_2 into high-value products in a circular economy [7]. In this context, *waste CO_2* refers to CO_2 recovered from flue gases at industrial scale, captured from the atmosphere, or separated from biomass gasification or biogas, which is in turn produced through the anaerobic decomposition of organic residues by microorganisms [8]. While separation efficiency remains one of the main challenges of CO_2 capture technologies [9], large-scale CO_2 utilization from flue gases could produce more conversion products than the market can absorb in early phases [10], whereas localized integration of methanol synthesis with biogenic CO_2 from organic wastes provides a feasible, carbon-neutral alternative [11]. Finally, by offering a valuable solution to convert carbonaceous waste, biomass, and hydrogen into a versatile liquid energy carrier, methanol synthesis overcomes the technical limitations of hydrogen with respect to infrastructure and transport feasibility [12].

The conversion of CO_2 and H_2 to methanol is described by the following equilibrium reactions [13]:

$$CO_2 + 3H_2 \leftrightarrow CH_3OH + H_2O, \quad \Delta H_r^0 = -50\ kJ\ mol^{-1} \tag{1}$$

$$CO_2 + H_2 \leftrightarrow CO + H_2O, \quad \Delta H_r^0 = 39\ kJ\ mol^{-1} \tag{2}$$

$$CO + 2H_2 \leftrightarrow CH_3OH, \quad \Delta H_r^0 = -91\ kJ\ mol^{-1} \tag{3}$$

Methanol synthesis from CO_2 (1) is accompanied by the reverse water-gas shift reaction (RWGS) (2), while reaction (3) represents the standard methanol synthesis from carbon monoxide (CO). In contrast to the exothermic methanol synthesis reactions (1)(3), the RWGS reaction (2) is endothermic. Hence, methanol synthesis is thermodynamically favored at lower temperatures, whereas CO production through the RWGS reaction is favored at higher temperatures. Another difference is that both methanol synthesis reactions are characterized by a reduction in volume, and thus favored at high pressures. Considering these thermodynamic constraints, industrial methanol reactors operate since the 1960s at temperatures between 200 and 300 °C and pressures ranging from 50 to 100 bar with a gas mixture of CO, CO_2 and H_2 reacting on a fixed copper/zinc oxide/aluminum oxide ($Cu/ZnO/Al_2O_3$ or CZA) catalyst bed [13,14]. In this process, CO_2 conversion to methanol (1) is considered as the result of Eqs. (2) and (3). CO_2-based methanol reactors were widely investigated over the years in parallel to methanol synthesis from syngas, showing feasible pathways of CO_2 valorization. Nevertheless, the commercialization of the process was limited by inadequate conversion and product purity [15]. The CO_2-to-methanol reaction produces large amounts of water (H_2O) as by-product, which inhibits methanol synthesis due to competitive H_2-H_2O and CO-formate species (HCOO*) adsorption on the catalyst surface [16]. Besides the problems related to catalyst optimization, methanol synthesis from waste CO_2 and renewable hydrogen poses significant challenges on reactor design, with significant drawbacks despite its attractiveness as a sustainable process. The main limitation of the CO_2-to-methanol process is its unfavorable thermodynamic equilibrium, resulting in low per-pass conversion, with high recycling rates of unreacted species. The highest conversion achievable according to thermodynamics at the temperatures of operation of the current metal-based catalysts (i.e., in the range 135–275 °C) is significantly lower than in the case of syngas-to-methanol [17]. This limitation arises from the high methanol selectivity achieved at temperatures that either inhibit CO_2 activation (<210 °C) or reduce the overall conversion efficiency (>300 °C). The latter is the case for indium-based catalysts, which, however, while highly selective towards methanol synthesis, rely on the zinc mining industry for their production, with energy-intensive indium extraction and refining due to its natural scarcity [18]. Additionally, decentralized methanol synthesis coupling renewable H_2 and biogenic CO_2 requires downscaling of the process due to the reduced H_2 availability from electrolysis and biomass reforming plants compared to the standard steam reforming of methane (CH_4) [19]. However, downscaling chemical reactors leads to performance losses, including limited availability of waste heat from steam

reforming processes, which are typically used to supply heat to raise steam used in a turbine connected to a compressor for high-pressure (HP) operations. The resulting purely electrical compression costs to increase methanol yield further hinder the economic viability of CO_2 hydrogenation on a small scale [11]. This calls for new technical solutions that allow to decrease the pressure level from the typical 6–8 MPa down to 2–3 MPa, corresponding to the typical outlet pressure of standard PEM water electrolysis, thus eliminating the need for hydrogen compression. Examples of unconventional reactors trying to face these challenges include highly-conductive structured catalysts for improved heat management [20], or thermally coupled dual reactors [21,22] with membranes [23] for product diversification and enhanced methanol synthesis efficiency through reactor heat transfer.

To overcome thermodynamics and shift reaction equilibrium towards enhanced product yield by other means than the pressure, removing at least one of the reaction products from the reactor is a promising approach. Removal of steam as a byproduct has been proposed as a process intensification strategy for many CO_2-based equilibrium limited reactions, including methanol synthesis, methanation, RWGS and DME production [24]. In the case of methanol synthesis, this has been experimentally investigated with integration of membranes [25], in-situ condensation of a CH_3OH-H_2O mixture [26], or by embedding the catalyst within a zeolite (13×), acting as a solid water sorbent in a fixed-bed reactor with batch-wise regeneration [27]. While membrane reactors experience sealing and material stability issues, the latter study demonstrated the feasibility of product adsorption to enhance reactivity, establishing sorption-enhanced (SE) methanol synthesis as a valuable approach to achieving higher methanol yield at low pressures. The development of a sorption-enhanced process depends on selecting a suitable sorbent with high selectivity for reaction products. This is crucial for reactor modelling and the effective design of downstream process units to enable techno-economic feasibility analysis [28].

The choice of the sorbent depends on the feedstock composition and operating conditions. For CO_2-based methanol reactors, the selective adsorption of water is beneficial because it reduces competitive adsorption on active sites and limits steam-induced sintering of metal-based catalysts, leading to catalyst deactivation [29]. Based on this, zeolite 3 A was identified as an ideal candidate due to its small pore size (3 Å), selectively excluding molecules with a larger kinetic diameter, such as CH_3OH and CO_2, from the adsorption process [30]. Additionally, the operation window of this material is in line with the requirements of standard methanol synthesis. The enhancement of CO_2 hydrogenation reactions by selective steam adsorption on zeolite 3 A has been experimentally validated for relevant process conditions [31,32]. SE methanol synthesis experiments demonstrated a temporary increase in methanol production and higher product purity, reducing the need for expensive CH_3OH-H_2O separation units [32,33]. As the advantages linked to the improved CO_2 conversion were limited by the short duration of the SE effect, these studies suggested to reduce the gas hourly space velocity (GHSV) and increase the reactor size for industrial applicability. However, this limits the options for a more compact reactor design, fast sorbent renewal and easy heat management. To outweigh the drawbacks of batch-wise operations in sorption-enhanced processes, efficient regeneration strategies such as parallel reactor setups or continuous sorbent processing have been proposed [34,35]. Specifically, the continuous transport of sorbent in and out of the reactor has been suggested for the coupling of biogas upgrading and Power-to-X (PtX) by designing the reactor with two parallel units in a pressure swing adsorption (PSA)-like process [36]. In this new reactor type, the uninterrupted circulation of sorbent is facilitated by keeping the catalyst bed in a bubbling fluidization regime. This method enables smaller reactors compared to fixed-bed configurations with sorbents, ensuring continuous operation by regenerating spent sorbent in a separate vessel rather than relying on multiple reactors with high catalyst demand per unit of methanol. The same concept of sorption-enhanced methanol synthesis in fluidized bed was already proposed for a thermally coupled reactor configuration and using zeolite 4 A as water sorbent [37]. Although molecular sieves 3 A and 4 A are considered highly suitable for steam removal [24], competitive adsorption of CO_2 on zeolite 4 A has been demonstrated [38]. Moreover, experimental investigation on adsorbents 4 A, 5 A and 13× confirmed co-adsorption of methanol, reinforcing the idea that zeolites with a pore size greater than 3 Å are less suitable for a CO_2-utilization process where a high product purity is targeted. Finally, materials other than zeolites, such as hydrotalcites and base metal oxides, are known to lose their steam adsorption capacity at the operating temperatures of the methanol synthesis process [39,40].

In this paper, we investigate the underlying aspects of sorption enhancement of CO and CH_3OH yield using molecular sieve 3 A in sorption-enhanced CO_2 hydrogenation to methanol for both fixed (FB) and bubbling fluidized (BFB) configurations of the catalyst-sorbent bed. This investigation, conducted in a lab-scale reactor operating at 3 bar, provides a preliminary proof-of-concept of an adsorptive BFB reactor and assesses its differences from a state-of-the-art FB reactor for selective steam removal. To facilitate later scale-up and maintain the research focus on the technology proof-of-concept, commercial catalyst and sorbent materials are employed. This work includes adsorption experiments to evaluate the water adsorption capacity by the selected sorbent across a temperature range relevant to methanol synthesis and in the presence of methanol. Standard methanol synthesis experiments were performed to establish baseline data on reaction yield and selectivity at the investigated pressure, serving as a reference for the sorption-enhancement experiments. Sorption-enhanced methanol synthesis was then explored under both fixed-bed and fluidized-bed conditions to understand the potential of reactor configuration in optimizing the sorption-enhancement process. The water uptake is quantified and compared to the additional CO and MeOH amount formed during the adsorption phase, which is not addressed in several experimental studies on SE methanol synthesis, including a comparison of the water breakthrough between FB and BFB reactors. Moreover, in a separate set of experiments, the sorbent's capacity and potential for co-adsorption of reaction products other than the target component is evaluated using the same facility and under the same conditions. To understand the impact of the targeted reactor pressure in industrial application (20–30 bar, similar to the hydrogen delivery pressure of standard electrolysis), a reactor model was developed, with adsorption parameters derived from the adsorption experimental data. Although the applied operating conditions in the lab-scale reactor resulted in high selectivity towards the RWGS reaction under both standard and sorption-enhanced methanol synthesis, a shift towards methanol formation is shown for higher pressures, and the methodology is still relevant to methanol enhancement strategies.

2. Materials and methods

2.1. Materials

KATALCO 51–102 was employed as a commercial $Cu/ZnO/Al_2O_3$ catalyst and molecular sieve 3 A as sorbent for sorption-enhanced methanol synthesis experiments. The catalyst and zeolite were purchased from Jonson Matthey and Jiangsu Zeochem Technology *Co.*, Ltd., respectively. CO_2 and H_2 for methanol synthesis were purchased in gas bottles, while liquid methanol for adsorption experiments was purchased from VWR Chemicals BDH, all with a purity ≥99.9 %. Ultrapure water with a conductivity of 18.2 MΩ × cm was acquired with an Arium® Pro system from Sartorius.

2.2. Experimental facility

The core of the experimental facility consisted of a vertical stainless-steel reactor with an internal porous plate as bed support, forming a reaction zone with a diameter of 21 mm and a length of 150 mm. Above the reaction zone, the cross-sectional area expands further into a

disengagement zone to facilitate fluidization. The vessel then narrows back towards the outlet, connected to a cross fitting that embeds two thermowells and the outlet pipeline. All the described parts of the vessel were electrically welded, resulting in a total length of 450 mm. The reaction and disengagement parts of the vessel were enclosed within an annular chamber, which was used to regulate the reactor temperature.

Preheated pressurized air flew through the chamber, providing temperature control based on real-time temperature measurements inside the bed. Specifically, two type K thermocouples positioned at the bottom and at the top of the bed through the thermowells (TT-609 and TT-604 in Fig. 1) were used for real-time temperature measurements inside the reactor during adsorption and non-SE methanol synthesis. Additional four type K thermocouples were placed inside the reaction zone and equally distributed in the second thermowell to acquire the temperature profile during SE methanol synthesis and verify isothermal conditions when fluidizing the catalyst-sorbent bed. Based on bed temperature readings, the air heater setpoint was manually adjusted, and the temperature of the hot air line was monitored via a dedicated thermocouple.

The pressure of the experimental facility was maintained by a back-pressure regulator. Dry gasses (CO_2, H_2, nitrogen, argon) and vapors (CH_3OH, H_2O) were mixed upstream a 4-valve system, which can direct the reactive flow from a bypass line to the reactor. The mixing and bypass lines were enclosed in an insulated chamber pre-heated at 270 °C. All flow rates, but CH_3OH, were regulated by Bronkhorst AG FV-201CV Mass Flow Controllers (MFCs). Liquid methanol, used to carry out co-adsorption experiments only, was injected in a preheated chamber by means of a syringe pump at a rate of up to 1 mL/min and carried as vapor by argon (Ar) in the mixing line. The initial condensate was collected at the bottom of the chamber and carried out by an exhaust line during the first phase of injection.

MFCs flow rates, temperatures, and pressure were controlled with a customized LabVIEW 2018 interface, allowing for monitoring, data acquisition, and high-speed control via the FPGA Module every 2 s. A mass spectrometer (Pfeiffer Vacuum GSD 301 O1, D-35614 Asslar) with a 10-s time interval was employed as a real-time analytical tool to quantify the relative abundance of known compounds based on their mass-to-charge ratio (m/z). The mass spectrometer (MS) was positioned downstream of a two-filter system and connected to both the reactor outlet and the bypass line by two manual valves, allowing it to measure concentrations from either path. Additionally, a Non-Dispersive Infrared (NDIR) sensor (Siemens ULTRAMAT 23) measured the volumetric concentrations of CO, CO_2, CH_4, and O_2 on the exhaust gas line, combining the outlet flows of the reactor and bypass after vapors condensation. The instruments were calibrated for three product gas compositions as described in the Supporting information. The MS calibration was used to determine the product gas composition at steady-state conditions during methanol synthesis experiments [41], as described in Section 2.3.2.

The described facility, built in-house, and connected analytics are schematized in the Fig. 1 below, showing the adsorption/reaction configuration of the 4-valve system. In this configuration, the reactive gas mixture, prepared in the mixing line, is fed from the bottom of the reactor. Meanwhile, inert gas flows through the bypass to maintain system pressure.

Pictures of the experimental facility are available in the Supporting information.

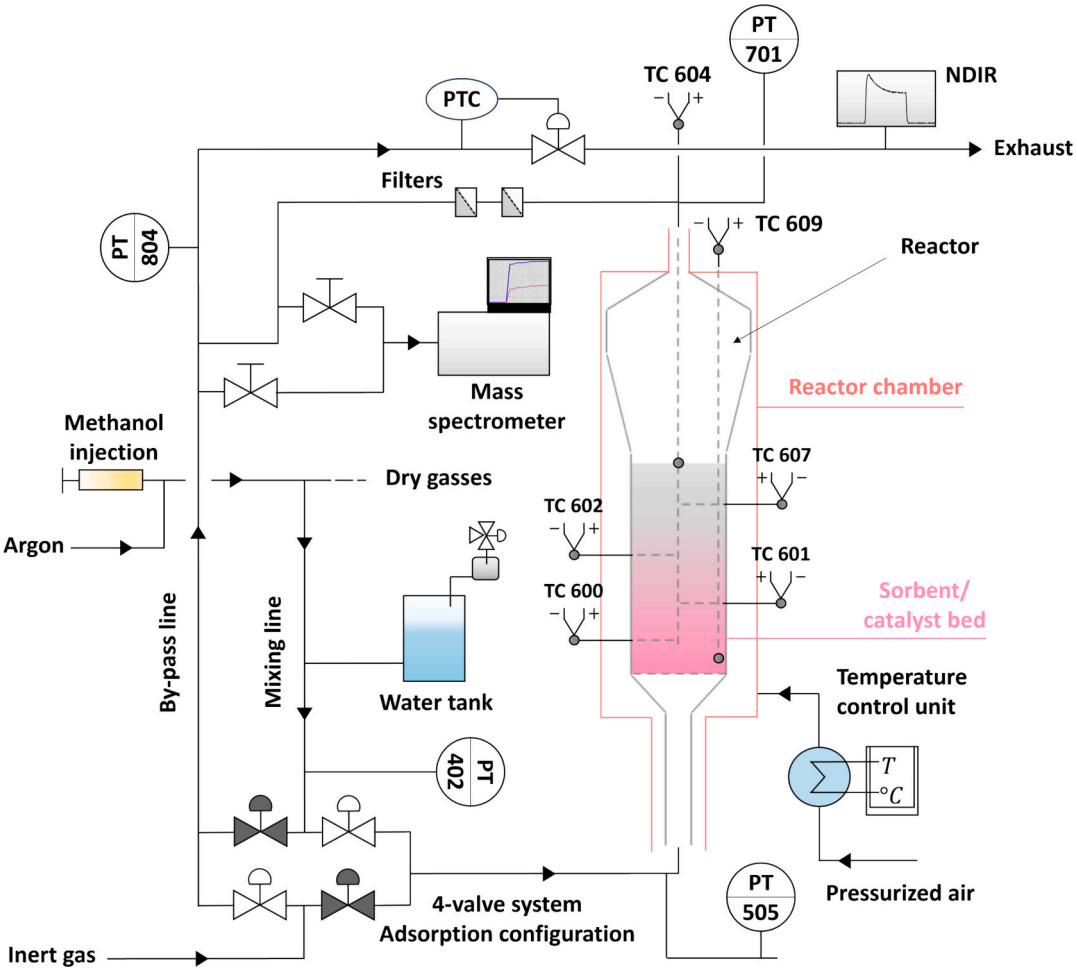

Fig. 1. Flow diagram of the testing facility.

2.3. Experimental campaigns and data analysis

The facility was operated with three different procedures based on the experimental breakdown reported in Table 1, containing all experimental conditions. These procedures are detailed in the following subsections.

The experimental studies were conducted on a lab scale at a constant absolute pressure of 3 bar. Tests on the zeolite's adsorption capacity towards water were performed for different temperatures, water partial pressures, and feed gas composition. Potential co-adsorption of CH_3OH was tested. Non-SE methanol synthesis was conducted in the temperature range dictated by the catalyst activation. SE methanol synthesis was conducted for a narrowed temperature range based on the findings from adsorption and non-enhanced methanol synthesis experiments, and for different catalyst-sorbent bed configurations.

2.3.1. Adsorption experiments

Before beginning the experiment, the sorbent was dried with 1 L/min of nitrogen (N_2) at 310 °C and the feed gas mixture was directed to the bypass. During this phase, the intensities indicative of complete adsorption and desorption of water and/or other species were established as reference for the experiment. As an example, Fig. 2 illustrates the signal intensities of H_2O, Ar and N_2 recorded during this phase at the bypass and reactor outlets for a gas mixture of 30 % water in argon at 250 °C. In the first 20 min, the gas feed was directed to the MS via the bypass. Over the first 8 min, only 100 % argon was recorded. Thereafter, 30 % water in argon was recorded for approximately 15 min. As the water signal increased, the argon signal decreased proportionally until reflecting the change in the gas composition. No adsorption occurred in the bypass, and the intensities were quantified with a known concentration through the flow rates recorded at the MFCs. This intensity was compared with the one measured at the reactor after sorbent saturation when the water signal broke from its minimum value and attained a higher stable intensity. A tolerance of $\pm 1.5 \times 10^{-9}$ was applied to the reference values for both adsorption and desorption. After the bypass measurements, the MS was connected to the reactor outlet, where 100 % N_2 was detected and the water signal was monitored for approximately 30 min to ensure baseline conditions.

At this point, the reactor temperature was regulated to the desired profile for the experiment, which starts when the feed gas is redirected from the bypass into the reactor and the inert gas to the bypass (adsorption configuration shown in Fig. 1). The intensities recorded at the reactor outlet during the experimental phase involving a gas mixture of 30 % water in argon at 250 °C are reported in Fig. 3. The moment an increase in the argon signal and a corresponding decrease in the nitrogen signal were detected marks the point when adsorption begun to be recorded. As the sorbent-free sites were filled with H_2O, no changes were observed in the water signal, and 100 % of argon was registered. The water breakthrough occurred when the sorbent was saturated until the signal intensities adjusted back to 30 % H_2O in Ar. The breakthrough curve was linearly rescaled using water flow rates (g/h) corresponding to steady-state intensity values within the baseline range established during the pre-experimental phase for complete adsorption and desorption. Baseline intensities were averaged from the differences between consecutive data points, and all values above the intersection of the upper average line with the breakthrough curve were excluded to remove outliers caused by fluctuations in the H_2O signal at steady-state, observed for water contents above 20 %. The first intersection between the upper average line and the adsorption curve at steady-state returned the final adsorption time, over which the breakthrough curve was integrated to calculate the water uptake (grams of adsorbed water). This, divided by the grams of loaded sorbent, returned the water adsorption capacity.

The steady-state condition was registered for a series of consecutive stable values (over 15 min in Fig. 3) before starting desorption, which was performed with 1 NL/min of argon at 310 °C and characterized by a decrease in the water signal over approximately 30 min. The times indicated for the experimental phase varied under different operating conditions.

The analysis focused on the variations in the signal attributed to the water molecule ions only, provided the absence of gas matrix effects, thus interfering effects from the surrounding gas environment that could alter the ionization efficiency, signal intensity, or mass accuracy of the water ions. Moreover, it was assumed based on the specifics of the employed MS that no other compounds contributed to the intensity of water at the mass charge ratio of 18. For co-adsorption experiments involving CH_3OH and H_2O, the methanol contribution of 2 % intensity at the m/z 18 was considered as negligible. This was justified by the chosen experimental conditions for co-adsorption experiments, involving the same partial pressure of 0.6 bar for CH_3OH and H_2O.

2.3.2. Methanol synthesis experiments

The catalyst activation process consisted of the following steps: a) Heating the reactor from ambient temperature to 160 °C under a flow of Ar and H_2, with the hydrogen partial pressure maintained below 200 mbar; b) gradually increasing the H_2 partial pressure in controlled steps: two increments of 50 % followed by one increment of 35 %, resulting in an approximate H_2 partial pressure of 1 bar; c) raising the reactor temperature from 160 °C to 250 °C; d) maintaining the temperature at 250 °C for 1 h to complete the activation. This procedure was preferred to the usual industrial activation protocol, optimized for methanol synthesis from CO, as it secures a more controlled nucleation and dispersion of metallic Cu particles without destabilizing the ZnO structure during the Cu-ZnO interaction [42]. Once the catalyst was active, the reactor temperature was adjusted to the experimental value. Next, the feed gas was adjusted to a reactive mixture of 0.2 NL/min CO_2, 0.65 NL/min H_2 and 0.15 NL/min Ar. The reaction took place for different temperatures in the catalyst activation range of 200–300 °C. For each temperature, stable signals of CO and CO_2 at the NDIR were measured for more than 10 min before adjusting the temperature to the next experimental value. At the end of the experiments, the reactive mixture was redirected to the bypass, and the catalyst was flushed with 1 L/min of argon. This phase can be considered as an empty bed experiment, in which the composition of the feed gas mixture flowing in the bypass was

Table 1
Breakdown of experiments based on the experimental class, reactor conditions, and intended output.

Class	Pressure [bar]	Temperature range [°C]	Feed gases	Bed configuration	Study objective
Adsorption	3	220–280	CH_3OH, H_2O, Ar H_2O, Ar CH_3OH, Ar	FB (16.3 g 3 A, 21 cm^3)	CH_3OH and H_2O adsorption capacity
Methanol synthesis	3	220–280	20 mol% CO_2, 65 mol% H_2, 15 mol% Ar	FB (22.2 g CZA, 21 cm^3)	CH_3OH vs CO yield and reaction selectivity
SE methanol synthesis	3	220–250	20 mol% CO_2, 65 mol% H_2, 15 mol% Ar	FB (21.5 g CZA, 21 cm^3, 16.9 g 3 A, 21 cm^3) BFB (10.9 g CZA, 10 cm^3, 8.3 g 3 A, 10 cm^3)	CH_3OH vs CO yield and reaction selectivity | H_2O adsorption capacity

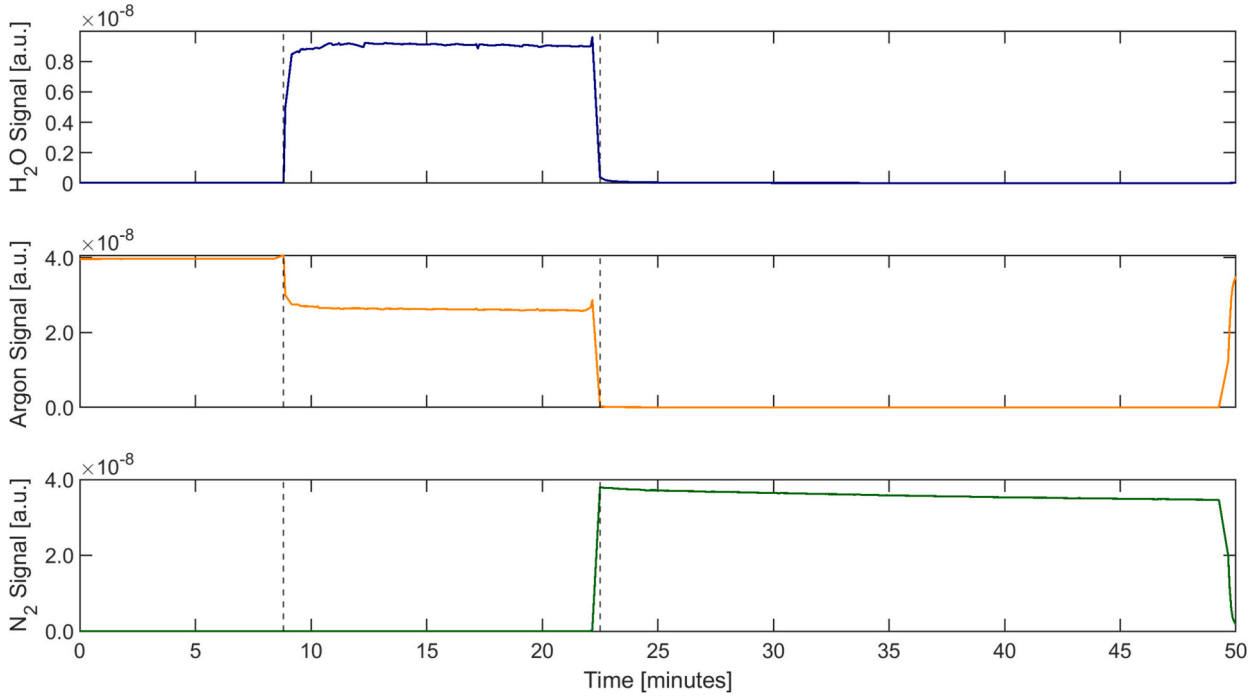

Fig. 2. Intensities of H_2O, Ar and N_2 signals recorded at the MS over time during the pre-experimental phase of the adsorption test with 30 mol% H_2O in Ar at 250 °C (pressure and bed configuration as in Table 1). From time 0 to the first vertical dotted line, 100 % argon was registered at the bypass outlet. Next, a feed gas mixture of 30 % H_2O in Ar was directed to the bypass, and the related intensities were recorded. The second vertical dotted line marks the point in time when the MS was connected to the reactor outlet and 100 % N_2 was registered.

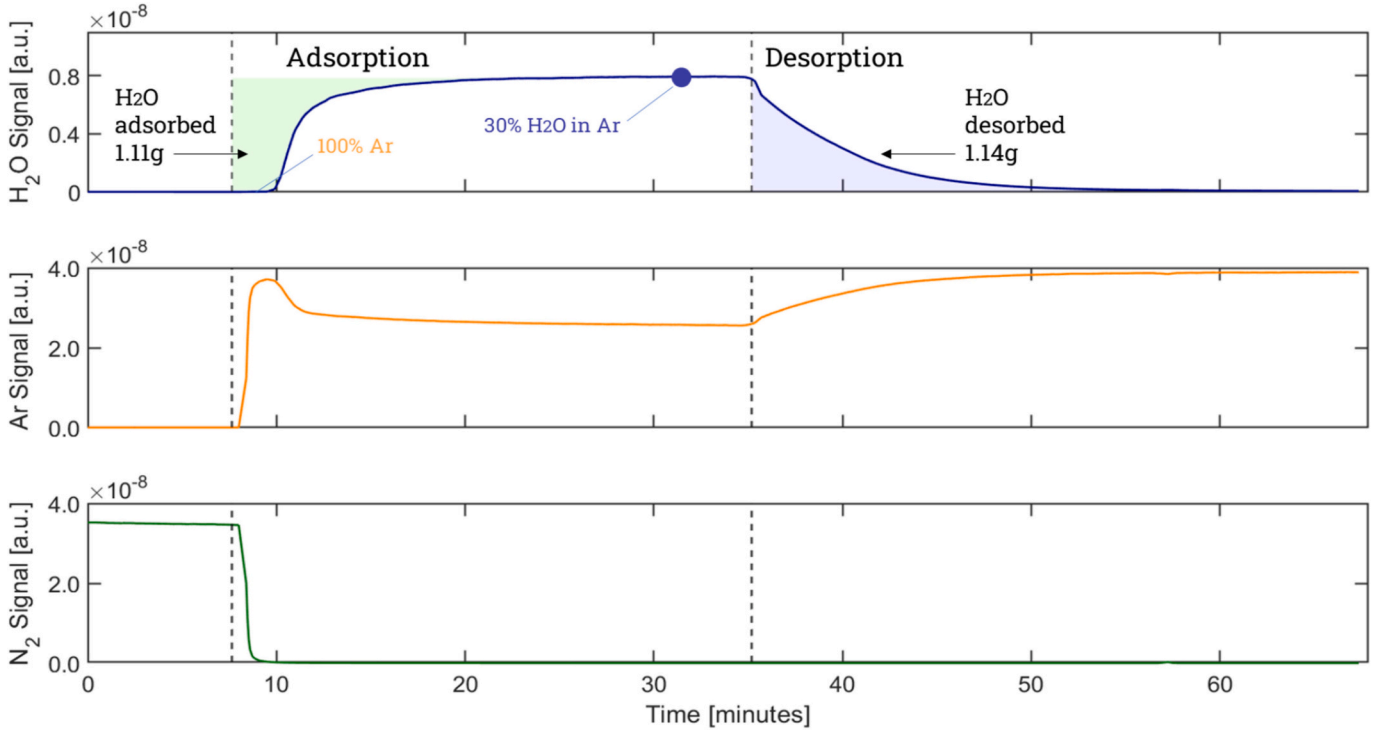

Fig. 3. Intensities of H_2O, Ar and N_2 signals recorded at the MS over time during the experimental phase of the adsorption test with 30 mol% H_2O in Ar at 250 °C (pressure and bed configuration as in Table 1). The dotted line represents the starting time for the adsorption/desorption phase. Shaded regions indicate the time windows integrated to obtain water uptake, which was computed on the curve linearly rescaled to water mass flow (g/h).

recorded at the NDIR and quantified back with the flow rates set at the MFCs for calibration.

The intensities measured at the MS for all the signals were translated to concentrations based on the mass spectrometer calibration results, which were represented as normalized relative sensitivities [41]. The calibration procedure to compute the normalized relative sensitivities is

detailed in the Supporting information, together with the determination of the product gas composition at equilibrium for methanol synthesis at 250 °C. In low-pressure (LP) methanol synthesis experiments, the high concentration of CO_2 in the product gas due to low conversion greatly affected the CO intensity at the same m/z 28, despite the CO_2 contribution (m/z 44) was subtracted from the CO ion current with, in this work, an 11.4 % correction. Therefore, the CO concentration measured at the NDIR was used to determine the overall CO_2 conversion and the selectivity of the methanol synthesis reaction, accounting for the removal of condensables from the gas mixture before reaching the sensor. Specifically, the CO_2 conversion rate to products was computed by interpolating experimental CO NDIR-based and CH_3OH MS-based data against theoretical values from the carbon balance for a theoretical CO_2 conversion vector ranging from 0 to 100 % with 0.1 % steps. An initial guess for the selectivity towards the RWGS reaction was set at 0.5 %. If the initial selectivity guess was not representative of the actual experiment, the conversion rate computed on the outlet CO concentration at the NDIR differed from that computed on the outlet CH_3OH concentration through the MS data. Given the difference between the CO_2 conversion metrics derived from CO and CH_3OH concentrations, the selectivity was optimized to minimize that difference. Once the right selectivity was determined, the carbon balance was used to recalculate the gas composition at the reactor outlet for the other species and rescale the mass spectrometer signals accordingly. Deviations of the MS-based CO_2, H_2, H_2O and Ar molar fractions from the theoretical carbon balance returned an overall averaged root mean squared error (RMSE) of 6 %. Finally, the methanol and CO yields were computed using the following formula:

$$Y_i = \frac{F_{i,outlet}}{F_{CO_2,inlet}} \cdot 100, \quad i = CH_3OH, CO \tag{4}$$

Additional details on the methodology for data analysis from independent measurements at the MS and NDIR are given in the Supporting information (graphic example and methodology flow chart).

2.3.3. Sorption-enhanced methanol synthesis experiments

The sorption-enhanced methanol synthesis was performed for a fixed and fluidized bed mixture of catalyst and sorbent in a volumetric ratio of 1:1 under 220, 235 and 250 °C. The catalyst was used in cylindrical pellet form (average diameter 5.5 mm) and the sorbent in spherical bead form (diameter 1.6–2.6 mm) as supplied, without grinding, for the fixed-bed experiments. The uniform distribution of the fixed bed was verified before and after the experiments with an endoscope. For the fluidized-bed experiments, the catalyst was ground and sieved to an 80–160 μm sample size, while the sorbent was ground and sieved to 125–250 μm to achieve a fluidization number between 2 and 3, corresponding to a bubbling fluidization state. The size difference between catalyst and sorbent particles ensured similar fluidization velocity of the two particle types, being the sorbent of lower density compared to the catalyst. Specifically, the minimum fluidization velocity of the mixture was calculated using the Ergun equation for fixed-bed pressure drop and equating it to the buoyancy-reduced gravitational force on the bed cross-section. The calculation was verified with pressure versus flow rate measurements of dense black sand particles (mimicking the CZA catalyst) and lighter, smaller γ-alumina particles (mimicking the sorbent), as performed in previous work to categorize the bed material for BFB reactor studies [43]. The fluidization was established by introducing the gas mixture from the bottom of the reactor. Additionally, the fluidization of the actual catalyst-sorbent bed was observed using a transparent plexiglass tube with the same diameter as the reactor and by applying the same superficial gas velocity as used under reactor operating conditions before loading it for the experiments. This preliminary test confirmed uniform distribution of the fluidized bed and Geldart type A/B behavior [44] prior to performing sorption-enhanced methanol synthesis. Compared to the FB configuration, the volume of catalyst and sorbent was proportionally reduced by half to prevent material loss from the reactor, as the fluidization pre-test revealed that the bed height more than doubled under fluidized conditions.

Prior to SE methanol synthesis, the pre-experimental phase described in Section 2.3.1 was conducted with 1 L/min of argon at 310 °C. When the pre-experimental phase was complete, the reactor was cooled down to 20 °C to start catalyst activation as described in Section 2.3.2. When both sorbent and catalyst were active, reactor temperature was brought to setpoint. The experiment started when the feed gas composition defined in Section 2.3.2 flew into the reactor. During the reaction, CH_3OH and H_2O signals were monitored through the MS, while CO_2 and CO outlet concentrations were monitored at the NDIR. Steady-state conditions were maintained for a series of consecutive stable values before starting desorption, which procedure is detailed in Section 2.3.1. Finally, the feed gas mixture was switched to the bypass to verify the calibration of the NDIR.

The analysis procedure for sorption-enhanced methanol synthesis experiments employed the methodology outlined in Section 2.3.2 to determine the gas composition at steady-state conditions for all species. This occurred after the sorption-enhancement effect ended due to sorbent saturation. At this point, the CO and CH_3OH signals measured by the NDIR and MS stabilized, decreasing from a maximum peak in intensity to a steady-state value representative of synthesis conditions without adsorption. The opposite stabilization trend was observed for the water signal at the mass spectrometer, which followed the behavior illustrated in Fig. 3. To define this final equilibrium state, the mean intensity of the final 30 data points was calculated for all signals. As detailed in Section 2.3.1, the signal was mapped to flow rates using a linear transformation between the minimum signal value and the equilibrium intensity at steady state, for which the corresponding flow rate in NmL/min was determined using the data reconciliation method explained in Section 2.3.2. While the linear mapping of H_2O and CH_3OH was performed at the mass spectrometer, the sorption enhancement of CO was computed on the NDIR curve, mapping the concentrations in mol.% the same way to obtain the production rates in NmL/min. This analysis was needed to differentiate between two integration regions below the CO and CH_3OH profiles. The area between the steady-state baseline and the maximum production rate represents the sorption-enhanced region, identified with positive deviations in the curve when resting the equilibrium baseline. This region is characterized by a peak in both CH_3OH and CO curves, which was used to analyze the peak performance of the sorption enhancement. The area below the steady-state baseline represents the standard conversion region without adsorption. The calculated areas returned the additional amount of methanol and CO produced due to sorption enhancement. The first change in the signals, determining the start of the experiment, was detected when the smoothed derivative of the signal, thus the rate of change, exceeded 50 % of the standard deviation of the derivative, indicating that the methanol and CO concentrations begun to increase noticeably. The area under the curve for the standard conversion (SC) region was computed using the following formula, assuming the CH_3OH and CO production rates at the end of sorption enhancement remain constant:

$$Area_{SC} = F_{i,outlet} \cdot \left(t_{SC,end} - t_{SC,start}\right), \quad i = CH_3OH, CO \tag{5}$$

The sorption-enhancement contribution ηSE to the total CH_3OH and CO production was then calculated as follows:

$$\eta SE = \frac{m_{i,SE}}{m_{i,SE} + m_{i,SC}} \cdot 100, \quad i = CH_3OH, CO \tag{6}$$

Finally, the water uptake was computed as the area between the breakthrough curve of H_2O and a baseline representing the adsorption at steady-state conditions, as described in Section 2.3.1. The water uptake was compared to the amount of additional CH_3OH and CO produced during the sorption-enhancement phase to quantify the impact of water removal on product yield.

2.4. Mathematical model

A dynamic one-dimensional model for the FB reactor with sorption enhancement was developed to provide a tool for space-time analysis and process scale-up. The material balance equation for each species i is as follows:

$$\frac{dF_i}{dt} = -v_G\frac{dF_i}{dz} + v_G(1-\varphi)\rho_C(1-\varepsilon)A\sum_{j=1}^{NR}\nu_{ij}r_j - \varphi\rho_A(1-\varepsilon)Av_G\frac{dq_i}{dt} \quad (7)$$

In Eq. (7), the gas velocity term v_G was adapted to account for the non-ideal flow behavior in the laboratory equipment. It was derived from the empty tube velocity v_{et} according to the following formula:

$$v_G = v_{et} \bullet \frac{t_{et}}{\langle t\rangle} \quad (8)$$

where t_{et} is the empty tube residence time and $\langle t\rangle$ is the average residence time in the lab-scale reactor obtained from experimental data.

The adsorption loading q_i in Eq. (7) is identically equal to zero for all species except H_2O. For water, it was obtained by integrating the following expression for the linear driving force (LDF) model of adsorption ($q_{H_2O} = q$ in the following):

$$\frac{dq}{dt} = k_a(q^* - q) \quad (9)$$

The equilibrium adsorbent loading q^* was determined from the saturation capacity m_{H_2O} through the single-site Langmuir isotherm of adsorption:

$$q^* = \frac{m_{H_2O}b_{H_2O}P_{H_2O}}{1 + b_{H_2O}P_{H_2O}} \quad (10)$$

where b_{H_2O}, the equilibrium constant, is temperature-dependent and follows the van't Hoff relation:

$$b_{H_2O} = b^0_{H_2O}\exp\left(-\frac{\Delta h^{ads}_{H_2O}}{RT}\right) \quad (11)$$

The linearization of Eq. (10), combined with experimental measurements of adsorption capacity as a function of varying water partial pressure, allowed for the determination of the parameters m_{H_2O} and b_{H_2O} for use in the model. Knowing the heat of adsorption of water on zeolite 3 A from literature [45], the Langmuir fitting parameter $b^0_{H_2O}$ was calculated. The single-component adsorption considered in the Langmuir linearization to compute the parameters was experimentally validated, confirming the absence of competitive adsorption by methanol.

The mass transfer coefficient k_a in Eq. (12) accounted for resistances from micropore diffusion and is expressed as [46]:

$$k_a = \frac{15\mathscr{D}_c}{r_c^2} \quad (12)$$

The model is pseudo-homogeneous, assuming uniform adsorption on the sorbent and negligible intra- and interphase diffusion resistances. The plug flow assumption was used, where flow is axially dominant with no back-mixing and negligible radial concentration gradients, justified by the small reactor diameter. Changes in molar flow along the reactor length were calculated based on axial velocity, with spatial derivatives computed using a 1st-order, backward finite difference scheme, as indicated below, where x represents any quantity that varies with axial position:

$$\left.\frac{dx}{dt}\right|_{z_k} = \frac{x|_{z_k} - x|_{z_{k-1}}}{z_k - z_{k-1}} \quad (13)$$

The model assumes negligible axial and radial mass and heat dispersion, with convection dominating the system. This enabled it to simulate realistic reactor behavior while maintaining computational simplicity. In fact, the reactor operated under conditions of high Péclet number, ensuring convection-dominated transport.

The kinetic model used in this study is the one developed by Graaf et al. [47], incorporating three macroscopic reactions: the hydrogenation of CO_2 to methanol, following the reaction rate Eq. (14), the RWGS reaction, following Eq. (15), and the hydrogenation of CO to methanol, following Eq. (16). The kinetic parameters characterizing the rate expressions are those estimated by Maksimov et al. [32], with experiments conducted on a commercial CZA catalyst at pressures ranging from 20 to 60 bar and temperatures between 210 °C and 270 °C. To account for the different catalyst used in this work (more selective to methanol), the rate constant for the methanol synthesis reactions and RWGS were modified through the fitting parameters α_MeOH and α_RWGS, as reported in the following equations:

$$r_1 = \frac{\alpha_{MeOH}k_1K_{CO_2}\left(P^{\frac{3}{2}}_{H_2}P_{CO_2} - \frac{1}{K_1^{eq}}\frac{P_{CH_3OH}P_{H_2O}}{P^{\frac{3}{2}}_{H_2}}\right)}{(1 + K_{CO}P_{CO} + K_{CO_2}P_{CO_2})\left(\sqrt{P_{H_2}} + \frac{K_{H_2O}P_{H_2O}}{\sqrt{K_{H_2}}}\right)} \quad (14)$$

$$r_2 = \frac{\alpha_{RWGS}k_2K_{CO_2}\left(P_{H_2}P_{CO_2} - \frac{1}{K_2^{eq}}P_{H_2O}P_{CO}\right)}{(1 + K_{CO}P_{CO} + K_{CO_2}P_{CO_2})\left(\sqrt{P_{H_2}} + \frac{K_{H_2O}P_{H_2O}}{\sqrt{K_{H_2}}}\right)} \quad (15)$$

$$r_3 = \frac{\alpha_{MeOH}k_3K_{CO}\left(P^{\frac{3}{2}}_{H_2}P_{CO} - \frac{1}{K_3^{eq}}\frac{P_{CH_3OH}}{\sqrt{P_{H_2}}}\right)}{(1 + K_{CO}P_{CO} + K_{CO_2}P_{CO_2})\left(\sqrt{P_{H_2}} + \frac{K_{H_2O}P_{H_2O}}{\sqrt{K_{H_2}}}\right)} \quad (16)$$

The partial differential equation model resulting from the equations listed above was solved using the finite differences method, with a linear discretization in the axial direction. The adsorbent-catalyst bed was divided into 100 sections to capture the spatial variations within the reactor, each represented by a set of ordinary differential equations (ODEs). The problem was solved in MATLAB with the built-in ode15s integrator, specifically designed for stiff problems.

3. Results and discussion

The results from pure adsorption experiments, as well as methanol synthesis with and without adsorption, are presented separately in the following subsections to facilitate clarity and comparison. Nominal temperature conditions and outcomes are listed in Table 3 (adsorption), Table 4 (methanol synthesis), Table 5 (SE methanol synthesis, equilibrium conditions) and Table 6 (SE methanol synthesis). The temperatures measured inside the reactor at 10 cm from the porous plate compared to the nominal temperatures are listed in the Supporting information.

3.1. Water adsorption

The adsorption experiment results are presented as the water adsorption capacity relative to the specific operating condition varied in each test. The water adsorption capacity was computed as specified in Section 2.3.1, and all the outcomes are summarized in Table 3. The left graph of Fig. 4 shows the H_2O adsorption capacity (wt%) measured in this work for single water adsorption from a gas mixture containing 20 % H_2O in Ar at 250 °C, as well as for a feed where an equivalent concentration of methanol was added (light magenta bar). In the same graph, single water adsorption is compared to the breakthrough data reported from van Kampen et al. at the same temperature and water partial pressure [30]. As for these literature results, the molecular sieve 3 A maintained high water selectivity without competitive adsorption of methanol, resulting in a consistent water uptake of approximately 5.5 %.

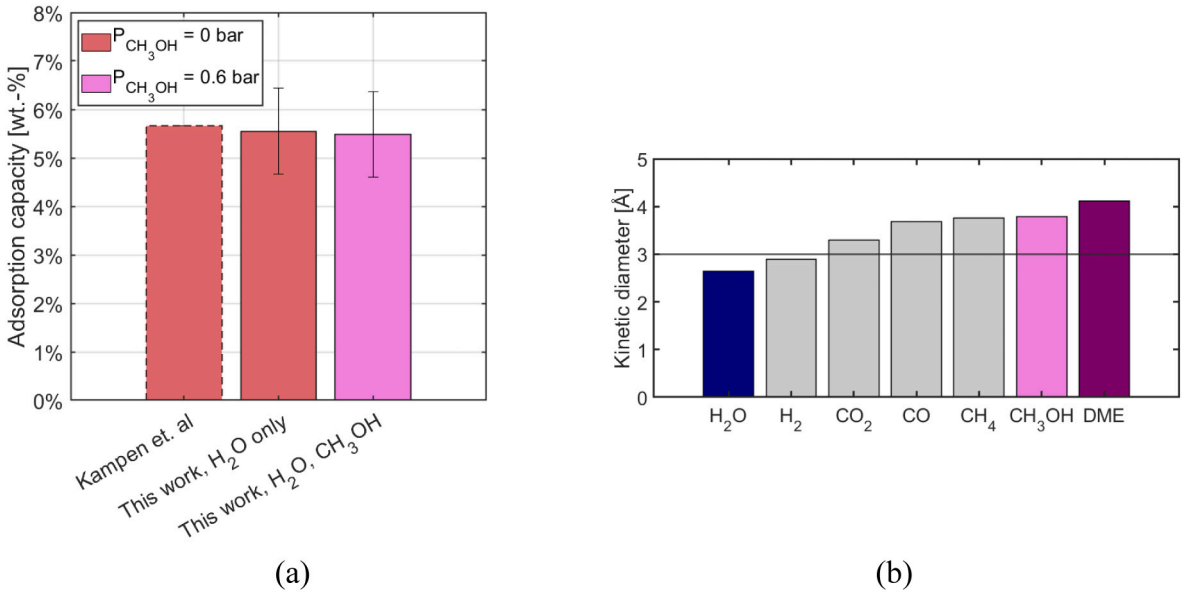

Fig. 4. (a) Water adsorption capacity measured in this work for single water adsorption (20 mol% H_2O in Ar at 250 °C) and for a feed with methanol added at an equivalent partial pressure, compared to data from van Kampen et al. [30] (pressure and bed configuration as in Table 1). Error bars represent the 95 % confidence interval of the mean, calculated using the Student's t-distribution for three replicate measures. (b) Kinetic diameters of various molecules relevant to steam adsorption enhanced processes, adapted from van Kampen et al. [30].

This outcome was verified with a final experiment quantifying the single methanol adsorption capacity of 3 A without water vapor in the gas feed, consisting of 20 % CH_3OH in Ar. No breakthrough, thus adsorption of methanol, was observed (results not shown). The results presented in this section are congruent with the higher selectivity for water exhibited by molecular sieve 3 A compared to other zeolites due to its small pore size of 3 Å, preventing molecules with a larger kinetic diameter from being adsorbed. This is explained in the right graph of Fig. 4, reporting the kinetic diameter of all the molecules generally involved in sorption-enhanced reactions as extrapolated from van Kampen et al. [24,30]. The graph highlights that only H_2O and H_2 molecules are characterized by a kinetic diameter lower than the pore size of zeolite 3 A, explaining the higher selectivity of the sorbent towards water. Potential adsorption of H_2 was not investigated in this work, as recent experimental research demonstrated that adsorption of H_2 is negligible under process conditions for temperature and pressure close to industrial methanol synthesis [32]. At the low pressures employed in this experimental work, the driving force for adsorption would be even smaller, making it likely for H_2 adsorption to remain negligible. Moreover, zeolite 3 A is designed to adsorb polar molecules [48], prioritizing the adsorption of water over non-polar or weakly polar molecules like H_2 and CO_2. Unlike large pore Faujasite (e.g., 13× zeolite), which features a different cationic structure that enhances CO_2 adsorption [49], 3 A exhibits low affinity for quadrupolar molecules, leaving little to no sorption capacity for CO_2. On the contrary, potential adsorption of CH_3OH by molecular sieve 3 A has been discussed with diverging points of view [50,51]. In this work, a peak in the DME following the breakthrough of water supported the idea of CH_3OH dehydration to form DME on the acidic sites of the zeolite, facilitated by the removal of water during the adsorption phase. However, due to the unvaried water adsorption capacity in presence of methanol, its adsorption in the micropores of the zeolite was excluded. Instead, it is assumed that the zeolite functions more as a catalyst than a sorbent for the dehydration reaction.

After confirming the selectivity of the adsorbent for steam removal, its ability to retain adsorption capacity across a temperature range relevant to the investigated process was verified. The results are reported in Fig. 5. The variation of 3 A's water uptake with temperature is again in good agreement with the breakthrough data extrapolated from literature, though a less sharp decrease was observed passing from 220 to 250 °C, corresponding to a 17 % loss in sorption capacity. A further temperature increase from 250 °C to 280 °C resulted in a more significant loss of 35 %. Overall, a total of 46 % of the water adsorption capacity was lost when the temperature was increased from 220 °C to 280 °C. The increasing differences between the water adsorption capacities calculated in this work and those reported by van Kampen et al. at lower temperatures may be attributed to the different material source and the resulting differences in material properties affecting water uptake. Generally, although standard methanol synthesis is typically conducted at 250 °C to maximize CH_3OH production rates, lower temperatures should be considered to optimize the sorption-enhanced process.

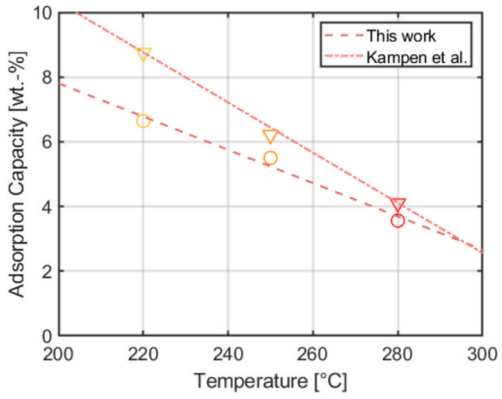

Fig. 5. Variation of molecular sieve 3 A's water adsorption capacity with temperature based on breakthrough experiments conducted in this work (○) and by van Kampen et al. (▽). Pressure and bed configuration as in Table 1.

Ultimately, the water adsorption capacity of molecular sieve 3 A was investigated at varying water partial pressures in argon at 250 °C to estimate the parameters for the Langmuir adsorption model. As illustrated in the left graph of Fig. 6, the adsorption capacity was measured for H_2O partial pressures ranging from 0 to 1.5 bar, yielding a maximum water uptake of 7.56 wt.-%. The resulting Langmuir correlation is also presented. Partial pressures exceeding 1.5 bar (corresponding to 50 %

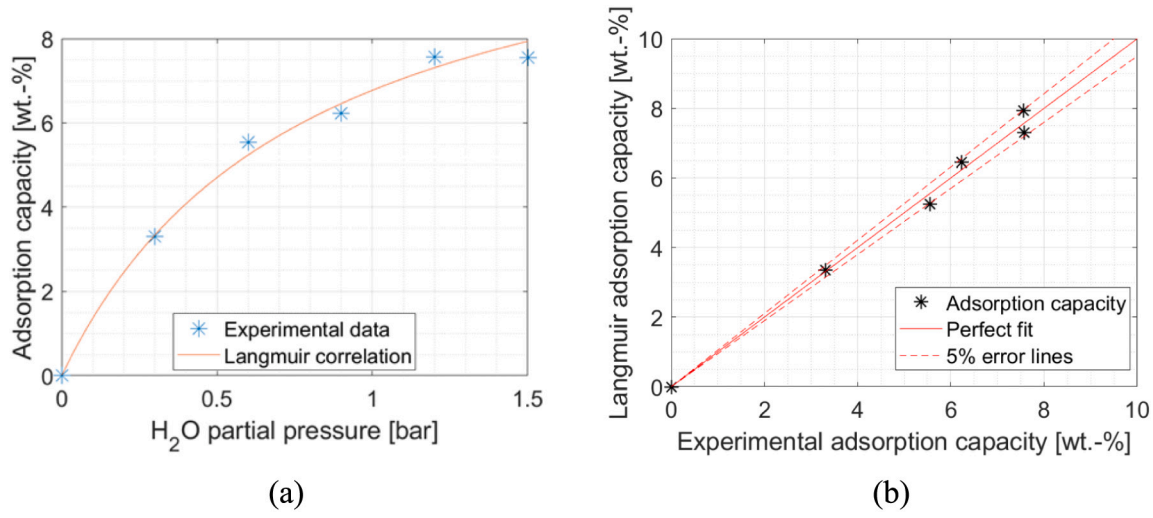

Fig. 6. (a) Breakthrough data (cyan *) and Langmuir of adsorption (red line) at 250 °C. (b) Parity plot: experimental breakthrough data (black *), perfect fit or parity line (red line), and ± 5 % error lines (red dashed lines) to prove the accuracy of the parameter estimation.

water content) resulted in significant fluctuations in the H_2O signal, which could not be reliably averaged or smoothed without introducing higher experimental error. The parity plot in the right graph demonstrates that the Langmuir model predictions align closely with the experimental data, showing a maximum deviation of 5 %. The estimated Langmuir parameters, listed in Table 2, were used in the reactor model for the simulations of SE methanol synthesis at a larger pressure range to show the scale-up feasibility.

3.2. Methanol synthesis

This section presents the results of methanol synthesis experiments conducted without adsorption, focusing on product yield and reaction selectivity as functions of temperature, as presented in Table 4. The reactor temperature was varied sequentially within the activation range of the commercial CZA catalyst (220–280 °C), leading to progressive changes in CH_3OH and CO production rates at equilibrium. As the reactor temperature increased, CH_3OH production decreased, while the production of CO and H_2O increased. These results served as a reference for comparison with SE methanol synthesis. Additionally, the findings were used to refine the optimal temperature range of investigation to enhance methanol yield and reduce the experimental matrix for subsequent experiments, similar to the approach applied for adsorption experiments.

Fig. 7 and Fig. 8 illustrate these trends as functions of bed temperature measured at a height of 10 cm. Fig. 7 highlights the effect of temperature on the selectivity between methanol synthesis and the reverse water-gas shift reaction. CH_3OH selectivity decreases with increasing temperature, while RWGS selectivity (and CO production) increases. This shift reflects the opposing thermodynamics of the reactions: methanol synthesis is exothermic and favored at lower temperatures, while the endothermic RWGS reaction is promoted at higher temperatures. Specifically, at 3 bar, methanol selectivity ranged from 6.3 % at 221 °C to 0.4 % at 273 °C, while RWGS selectivity spanned 93.4 % to 99.7 %. These results align with ASPEN simulations, which predict CH_3OH selectivity between 3.7 % (220 °C) and 0.3 % (280 °C). The higher experimental selectivity observed near 220 °C may be attributed to the tailored catalyst activation procedure detailed in Section 2.3.2 or the improved activity of the catalyst compared to its predecessors [52]. The observed methanol selectivity is also consistent with literature results on CO_2 hydrogenation to methanol over Cu–ZnO catalysts in

Table 2
Adsorption parameters estimated from breakthrough experimental data of water adsorption over molecular sieve 3 A at 250 °C and water partial pressures from 0 to 1.5 bar.

Adsorption parameter	Value		Reference
m_{H_2O}	12.10	[wt%]	This work
b_{H_2O}	1.273e-05	[1/Pa]	This work
$\Delta h^{ads}_{H_2O}$	- 78	[kJ/mol]	[45]
$b^0_{H_2O}$	2.072e-13	[1/Pa]	This work

Table 3
H_2O adsorption capacity on molecular sieve 3 A under all experimental conditions investigated in the pure adsorption experiments.

Nominal reactor temperature [°C]	H_2O partial pressure [bar]	CH_3OH partial pressure [bar]	H_2O adsorption capacity [wt.-%]
220	0.6	–	6.64
250	0.3	–	3.31
250	0.6	–	5.55
250	0.6	0.6	5.49
250	0.9	–	6.23
250	1.2	–	7.57
250	1.5	–	7.56
280	0.6	–	3.56

Table 4
Product yield and reaction selectivity as functions of temperature in methanol synthesis experiments without adsorption on a commercial $Cu/ZnO/Al_2O_3$ catalyst under constant pressure (3 bar), inlet flow rate (1NL/min) and inlet gas composition (20 mol% CO_2, 65 mol% H_2, 15 mol% Ar).

Nominal reactor temperature [°C]	CH_3OH selectivity [%]	CO selectivity [%]	Overall CO_2 conversion [%]	CH_3OH yield [%]	CO yield [%]
220	6.32	93.68	7.76	0.49	7.27
225	4.75	95.25	8.93	0.42	8.50
230	3.59	96.41	10.15	0.36	9.79
235	2.67	97.33	11.23	0.30	10.93
240	1.65	98.35	13.01	0.21	12.80
245	1.15	98.85	14.32	0.17	14.16
250	1.11	98.89	14.34	0.16	14.18
255	0.84	99.16	15.53	0.13	15.40
260	0.69	99.31	16.42	0.11	16.31
265	0.55	99.45	17.24	0.10	17.14
270	0.46	99.54	18.10	0.08	18.02
275	0.40	99.60	18.67	0.07	18.60

Table 5
Product yield and reaction selectivity at steady-state conditions after sorption enhancement as functions of temperature in SE methanol synthesis experiments under the conditions underlined in Table 4.

Bed type	Nominal reactor temperature [°C]	Overall CO_2 conversion [%]	CH_3OH yield at equilibrium [%]	CO yield at equilibrium [%]	CH_3OH selectivity at equilibrium [%]	CO selectivity at equilibrium [%]
FB	220	10.25	0.36	9.89	3.54	96.46
	235	13.84	0.24	13.60	1.70	98.30
	250	16.68	0.13	16.55	0.81	99.19
BFB	220	9.71	0.35	9.35	3.64	96.36
	235	12.80	0.19	12.62	1.46	98.54
	250	16.08	0.13	15.96	0.78	99.22

Table 6
Maximum product yield, total amount of CH_3OH and CO produced and contribution of sorption enhancement ηSE calculated from Eq. (6) as functions of temperature in SE methanol synthesis experiments under the conditions underlined in Table 4.

Bed type	Nominal reactor temperature [°C]	CH_3OH yield at peak [%]	CO yield at peak [%]	Total CH_3OH produced [mg]	Total CO produced [mg]	ηSE CH_3OH [%]	ηSE CO [%]
FB	220	0.47	15.85	25.10	967.30	13.60	16.90
	235	0.37	22.49	15.10	936.30	19.20	19.60
	250	0.24	28.67	7.40	977.10	21.50	20.20
BFB	220	0.57	17.26	26.20	699.30	17.30	17.30
	235	0.30	20.72	10.60	807.30	19.10	13.20
	250	0.20	26.51	4.30	573.60	22.50	18.30

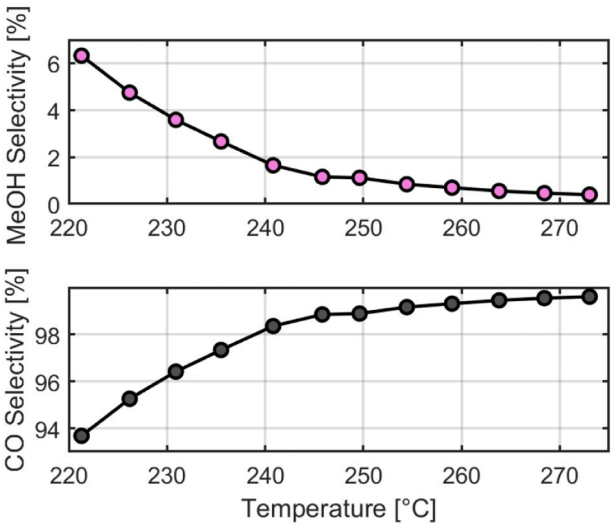

Fig. 7. Selectivity towards CH_3OH and CO production for a CO_2-based methanol reactor as a function of temperature over a commercial $Cu/ZnO/Al_2O_3$ catalyst at the constant pressure of 3 bar (inlet composition and bed configuration as in Table 1).

packed-bed reactors at near-atmospheric pressure, where values below 10 % were reported in the 190–250 °C range and approached zero at 250 °C [53]. These studies confirmed that at ~1 bar the reaction pathway is dominated by RWGS, with methanol selectivity decreasing as temperature increases. They further showed that catalyst support can influence selectivity by mitigating water inhibition. The sorption-enhanced approach presented in this paper tackles water inhibition directly through in-situ water removal, as presented in the next section, leading to even greater improvements under comparable conditions. Since pressure remains the primary lever to suppress CO formation and enhance methanol selectivity, complementary modelling work was conducted to extend the analysis, as discussed in Section 3.4.

Fig. 8 presents the overall CO_2 conversion and the corresponding variations in CH_3OH and CO yields as functions of temperature. The enhanced CO_2 conversion at higher temperatures aligns with the increased adsorption of H_2CO_2 intermediates on the catalyst [16]. CH_3OH yield at 3 bar was limited to a range of 0.5 % (221 °C) to 0.1 % (273 °C), while CO yield increased with temperature, ranging from 7.3 % to 18.6 %. These results are consistent with simulations, though the observed CO yield was lower than predicted. This discrepancy may further support the hypothesis of improved catalyst activation, which enhances methanol selectivity.

3.3. Sorption-enhanced methanol synthesis

Following the findings from the adsorption and standard methanol synthesis experiments, sorption-enhanced methanol synthesis was investigated in a narrowed temperature range (220–250 °C) to allow for higher adsorption capacity and higher methanol production rates. The results focus on the impact of sorption enhancement due to selective steam removal on extra product yield and added product quantity as a function of temperature, suggesting an adsorptive BFB reactor configuration, which could aid continuous sorbent regeneration. The outcomes are summarized in Table 5 for equilibrium conditions and in Table 6 for sorption-enhanced conditions. A complete table including the CH_3OH and CO amounts produced based on standard conversion and sorption enhancement is provided in the Supporting information.

3.3.1. Fixed-bed sorption-enhanced methanol synthesis experiments

To assess the sorption-enhancement effect resulting from water adsorption, the concentration profiles recorded by the MS and NDIR were analyzed and compared with those from standard methanol synthesis experiments. Fig. 9 presents the outlet trends for CO and CO_2 (a) as well as CH_3OH and H_2O (b) at the three investigated reactor temperatures: 220 °C, 235 °C, and 250 °C. In the left graph of Fig. 9, CO and CO_2 concentrations were recorded using the NDIR. Higher temperatures (indicated by the shift to darker colors) corresponded to higher CO concentrations and greater CO_2 conversion, as identified by the lower outlet concentration recorded for CO_2. This reflects the combined influence of the RWGS reaction and methanol synthesis. In the right graph, the MS intensities for CH_3OH and H_2O are presented, with the right y-axis adjusted to display negative intensities for an improved visualization. Higher temperatures (darker colors) corresponded to higher H_2O concentrations measured at steady-state conditions, and lower CH_3OH intensity. This observation aligns again with the thermodynamic

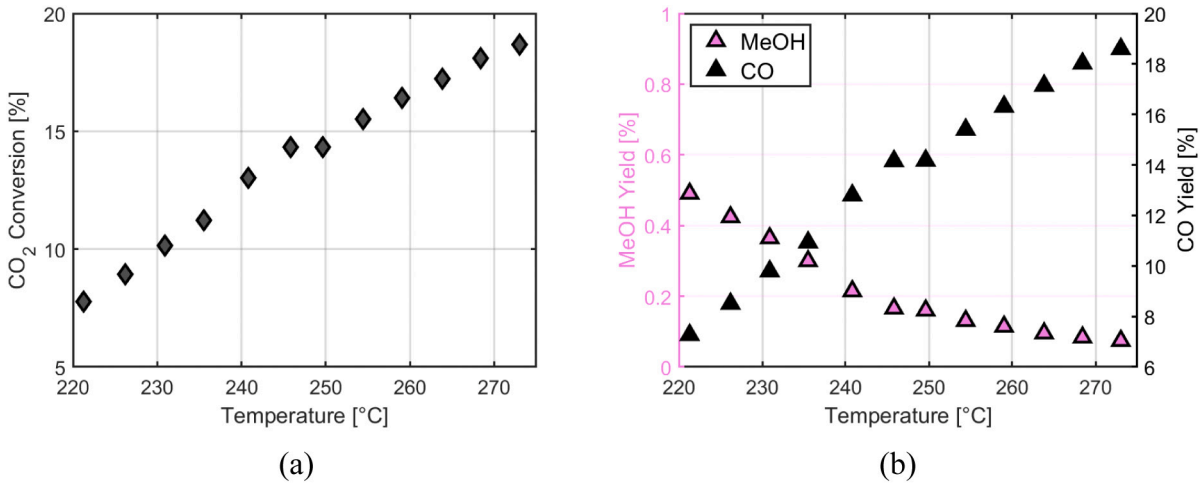

Fig. 8. Effect of temperature on CO_2 conversion (a) and product yields (b). The temperature range of 221 °C to 273 °C refers to the measurement using a thermocouple positioned at a bed height of 10 cm (inlet composition and bed configuration as in Table 1).

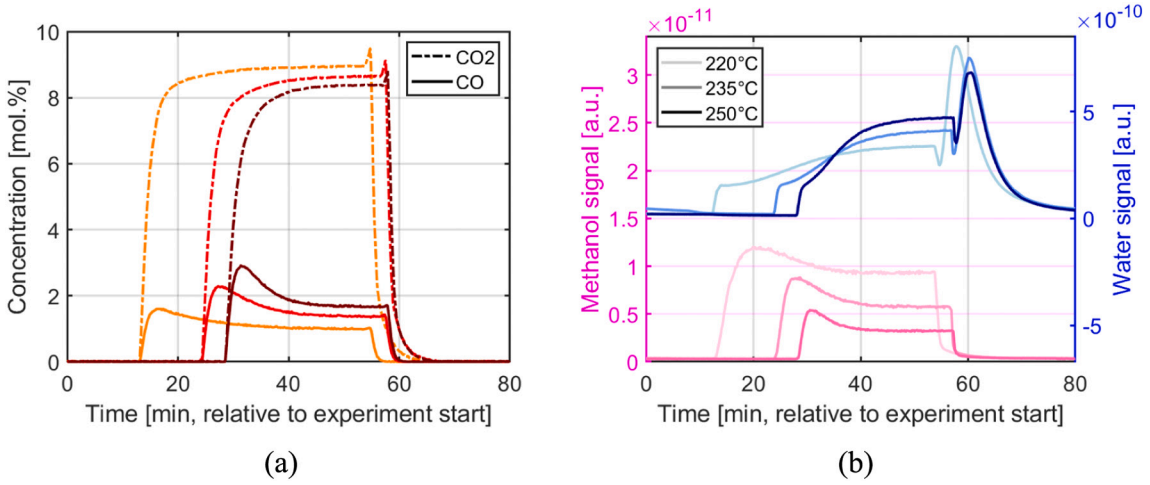

Fig. 9. (a) Time-resolved analysis of CO_2 (dashed lines) and CO concentrations (solid lines) in mol.% measured at the NDIR. (b) Time-resolved analysis of MeOH (light to dark pink solid lines) and H_2O (light to dark blue solid lines) signals measured at the MS. Both graphs refer to sorption-enhanced methanol synthesis followed by water desorption at 310 °C for a fixed-bed configuration of CZA (21.5 g)-3 A (16.9 g) mixture in 1:1 volumetric ratio. The shift in color from light to dark indicates the different temperatures at which the experiment was carried out, from 220 to 235 and 250 °C (inlet composition and pressure as in Table 1).

principles and reaction stoichiometry discussed for methanol synthesis without adsorption. A clear sorption-enhancement effect was observed at all temperatures, marked by peaks in CO and CH_3OH production, which diminished as equilibrium conditions were re-established due to sorbent saturation. At 220 °C, the sorption-enhancement effect was particularly pronounced due to the higher water adsorption capacity of the sorbent at lower temperatures. This is evident from the plateau in the H_2O signal and the sustained CH_3OH intensity, indicating a prolonged equilibrium shift facilitated by water removal. This effect was already observed by previous authors for CO_2 hydrogenation to methane [54,55]. At higher temperatures (235 °C and 250 °C), the sorption-enhancement effect was shorter, as the reduced water adsorption capacity accelerated the return to equilibrium, resulting in faster signal stabilization. As CO_2 concentration underwent a monotonous increase, its potential adsorption on the sorbent could be conclusively excluded. When the sorbent approached saturation, the H_2O signal progressively increased while the CH_3OH and CO signals decreased, stabilizing at the equilibrium value associated with the reactor temperature. A stable production rate over time for all reaction products was observed at the conclusion of the sorption-enhancement phase. To regenerate the sorbent, desorption was performed at a higher temperature before initiating the next experiment. In the right plot, the onset of water desorption is marked by a sharp peak in intensity as the temperature rises, indicating the release of H_2O from the sorbent. This is followed by a signal decrease over approximately 30 min as the desorbed water exited the reactor.

Once sorption enhancement was established, the additional production of CH_3OH and CO was quantified and compared to the water uptake, as outlined in Section 2.3.3. These results, illustrated in Fig. 10 across the three investigated temperatures, demonstrated the impact of water removal on shifting the equilibrium towards reaction products, as described by Le Chatelier's Principle. The additional CH_3OH and CO produced during the SE phase, quantified by the integrated areas, highlight this equilibrium shift. Although H_2O adsorption shifted the equilibrium position, the production of CH_3OH and CO remained governed by the reaction rates. During sorption enhancement, the transient peaks suggest that both methanol and RWGS reactions were primarily driven by the kinetic effect of H_2O removal, which temporarily altered the equilibrium and accelerated the rates of reaction. This enhancement is further evidenced by the progressive uptake of water in the adsorption graphs (right panels (c), (f), and (i)), which temporarily suppressed the inhibitory effect of H_2O on the metal catalyst. In summary, the transient

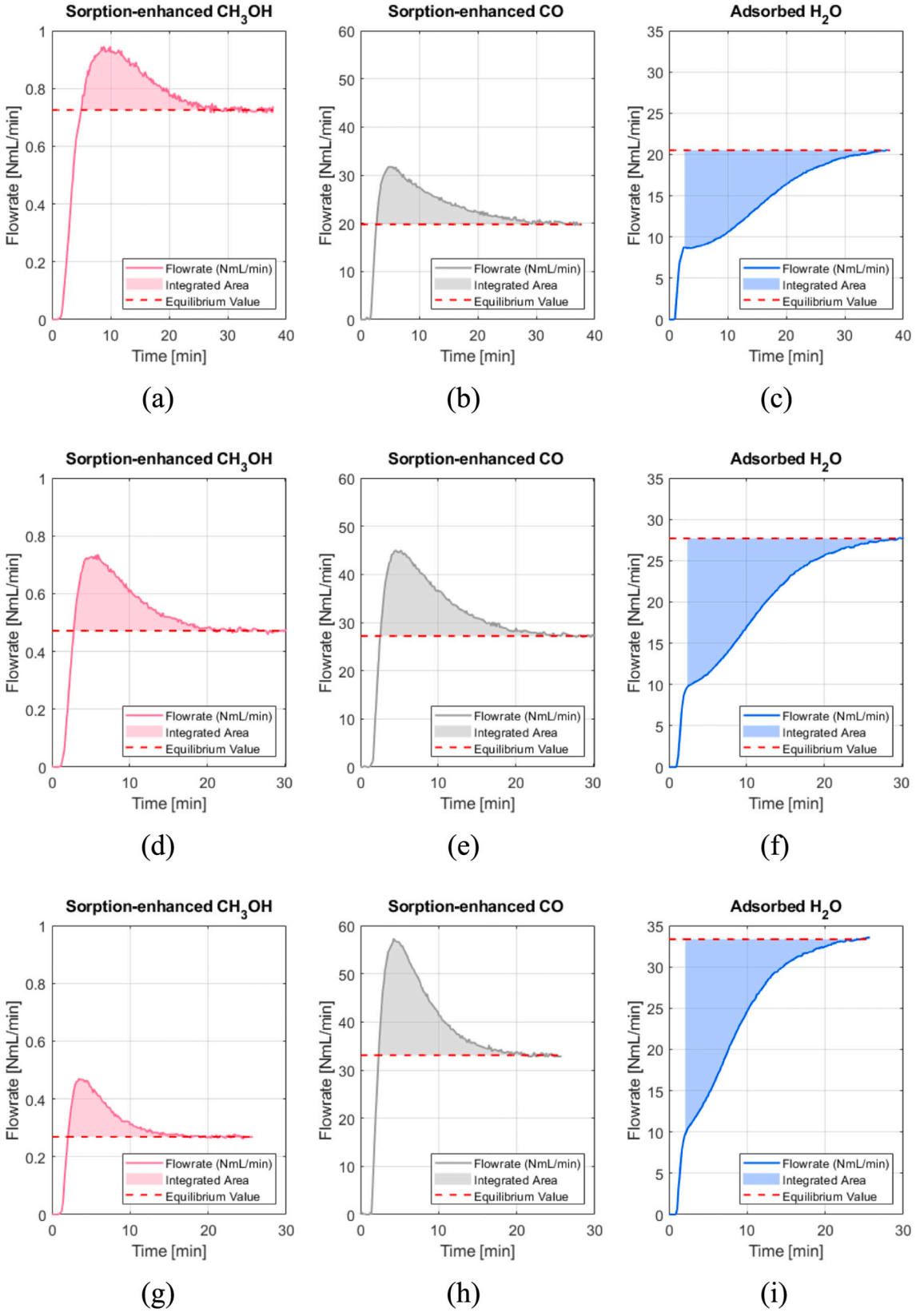

Fig. 10. Visual illustration of the quantified amount of sorption-enhanced CH_3OH and CO produced in comparison to the water uptake (adsorbed H_2O) at the reactor temperature of 220 °C (a) (b) (c), 235 °C (d) (e) (f), and 250 °C (g) (h) (i) for the fixed-bed configuration with 21.5 g CZA and 16.9 g 3 A (inlet composition and pressure as in Table 1). The outlet flow rate evolution over time and integration of the SE area were computed with the MS (CH_3OH and H_2O) and NDIR (CO) data after determining the equilibrium composition.

period was characterized by reaction rates momentarily exceeding those expected under equilibrium conditions due to water adsorption.

The impact of temperature on product selectivity is evident, with the methanol production at equilibrium decreasing at higher temperatures due to the exothermic nature of the synthesis reaction. The total CO production remained relatively stable (Table 6). Compared to the methanol synthesis experiments without adsorption (Table 5), the dominance of the reverse water-gas shift reaction, particularly at higher temperatures, was coupled with the increased consumption of H_2 on the catalyst during the sorption-enhancement phase, returning a final equilibrium state that favored CO selectivity. As more H_2 was consumed during the SE phase due to the accelerated reaction rates, its concentration in the gas phase lowered, while CO concentration increased thanks to water adsorption.

Despite higher CO flow rates observed at steady-state conditions as temperature increased from 220 °C to 250 °C (central panels (b), (e), and (h)), the duration of SE effect shortened, clarifying why the overall CO output, as presented in Table 6, remained consistent compared to CH_3OH. In fact, following the decrease at steady-state, the additional methanol produced through water removal decreased by more than 50 % from 220 °C to 250 °C, whereas the additional CO produced showed an overall increase of 20 %.

Interestingly, the contribution of sorption enhancement (ηSE) to methanol production (Eq. (6)), increased with temperature. This increase can be explained by the interplay of several effects. The total water uptake remained relatively constant across the temperature range due an improved CO_2-to-H_2O conversion but with a shorter adsorption time at higher temperatures, limiting the duration of the SE effect. This reduced the absolute amount of additional CH_3OH produced. Simultaneously, standard methanol production decreased significantly at higher temperatures due to unfavorable thermodynamics. As a result, the relative enhancement during SE became more pronounced at elevated temperatures. The combined effect of these trends - shorter SE duration, reduced total methanol production, and a larger relative enhancement - resulted in an increase in ηSE, as the contribution of the sorption enhancement became more significant relative to the total production. In the trade-off between absolute CH_3OH production and ηSE, operating temperatures between 220 and 235 °C are recommended to achieve a balance (left panels (a), (d)).

The ηSE contribution to CO enhancement also increased with temperature. Although water adsorption appeared to contribute more significantly to the RWGS reaction, ηSE values for CH_3OH and CO were comparable at 250 °C, reaching maximum values of 21.50 % and 20.20 %, respectively (Table 6). This trend suggests that the SE effect becomes more pronounced at elevated temperatures, driven by faster reaction kinetics and water removal shifting the equilibrium towards product formation. However, the higher SE efficiency at 250 °C was offset by the substantial drop in total methanol production, making this temperature less favorable for single-stage methanol synthesis.

At 250 °C, the additional CO mass produced during SE (977.10 mg) far exceeded the additional methanol mass (7.40 mg), indicating a process shift towards CO formation, as confirmed by previous experimental and modelling studies [32,36]. This opens the possibility of using CO as an intermediate for CH_3OH production in a two-stage process. In such a configuration, the first stage could operate at low pressure and 250 °C to maximize the synthesis of CO from biogenic CO_2, followed by a second stage at higher pressure to convert CO to methanol (Eq. (3)). This approach leverages the high CO yields observed during LP sorption enhancement while optimizing CH_3OH production in a subsequent HP stage (e.g., at the typical delivery pressure of 30 bar for a standard electrolyzer). For the methanol synthesis stage, operating at 220 °C–235 °C remains the most favorable, balancing total methanol yield and the benefits of the sorption enhancement.

The water uptake as represented in the right plots of Fig. 10 amounted for approximately 0.14 g of liquid water adsorbed. This amount did not correspond to the sum of additional CH_3OH and CO produced during SE, with a higher discrepancy for decreasing temperatures due to a lower amount of additional CO produced compared to the constant amount of water adsorbed. This is in line with a slower RWGS reaction kinetic, while water adsorption remains driven by its interaction with the sorbent, which is less temperature-dependent compared to the reaction rates. The fact that steam removal and product addition was not linearly related indicates that the sorbent must adsorb more H_2O than what is stoichiometrically produced to achieve the sorption enhancement indicated in Table 6. A constant amount of adsorbed water but greater enhancement of other reaction product is in agreement with previous findings on steam removal enhanced CO_2 hydrogenation [31]. Moreover, it was observed that the water adsorption process extended beyond SE, with a less sharp increase of H_2O to its steady-state value compared to the breakthrough over additional 5 to 10 min. This is because H_2O continued to be produced at equilibrium conditions, and the sorbent could still take up water as long as it had available adsorption capacity. However, the additional CH_3OH and CO production during the SE phase was limited to the time when the equilibrium was shifted significantly by water removal.

Fig. 11 illustrates the sorption-enhanced performance at peak conditions, showing that the maximum product yield for CH_3OH (a) could reach approximately 130–175 % of its equilibrium value across the temperature range of 220–250 °C. For CO (b), this factor lay between 160 and 173 %. The error bars in the figure (standard deviation) were derived from a dedicated repeatability test conducted at 250 °C, representing the most demanding case due to the lower methanol production. Three independent runs under identical conditions showed very small variations, with absolute standard deviations of approximately 0.01 % for methanol yields and similarly low values for other products, indicating good repeatability for all calculated quantities.

These peak performances align with the outlet performance metrics reported in previous SE studies conducted in fixed-bed reactors [32]. However, this parameter is only meaningful if the peak does not correspond to a relatively short transient behavior. Despite the promising results observed under peak conditions, the constraint of discontinuous operation due to sorbent regeneration after the sorption-enhancement phase persists. Extending the adsorption time by increasing reactor length at reasonable GHSV to achieve acceptable product yields would require a significantly larger quantity of sorbent material and result in prolonged regeneration times. This highlights the critical need for more efficient regeneration strategies, such as those proposed for fluidized-entrained bed reactors [34], which offer the potential for continuous operation and improved process scalability.

3.3.2. *Fluidized-bed sorption-enhanced methanol synthesis experiments*

The trend discussed for the FB sorption-enhancement results is consistent with what was observed for the BFB reactor, with close values at equilibrium, although only half of the bed material was used for the BFB experiments. The overall methanol produced as sum of the sorption-enhanced and standard conversion was sharply reduced with temperature, decreasing by more than 70 % from 220 °C to 250 °C.

However, in contrast to what was observed for the FB configuration, the additional amount of CO produced during sorption enhancement decreased passing from 220 °C to 235 and 250 °C.

Because of this decrease compared to the higher total amount of CO produced at 235 °C, the contribution of sorption enhancement ηSE to CO at this temperature lowered (Table 6). Nevertheless, since the relative SE contribution to methanol increased with temperature, ηSE values for both CH_3OH and CO are maximized at 250 °C, reaching maximum values of 22.50 % and 18.30 %. At 220 °C, these two values are equal, though the total CO produced during SE (699.30 mg) again exceeded the total amount of methanol (26.20 mg), confirming a higher enhancement of CO formation by selective removal of steam.

Despite an increasing peak performance and outlet flow rate at equilibrium with temperature, as highlighted by the central plots (b), (e), and (h) in Fig. 10 for the fixed bed, water adsorption was

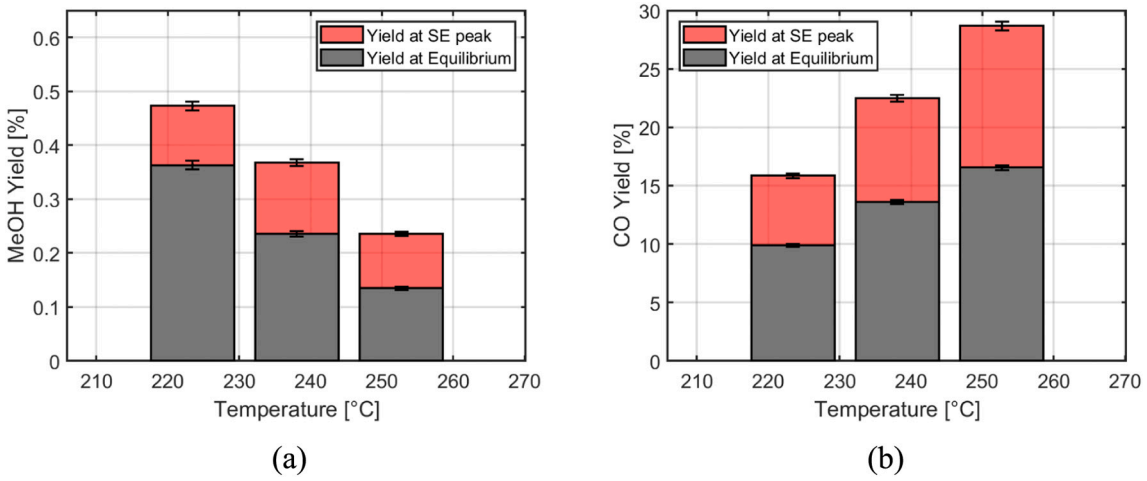

Fig. 11. (a) MeOH yield at the peak of sorption enhancement (red stacked bars) compared to the yield at equilibrium (gray bars) across the investigated temperatures of 220, 235 and 250 °C for a fixed-bed configuration of catalyst-sorbent. (b) Same comparison for CO yield. Error bars (standard deviations) were derived from a repeatability test at 250 °C.

characterized by a sharper breakthrough in the BFB configuration. This is evident when comparing the BFB results for the outlet flow rates of CH_3OH, CO and H_2O, along with integrated areas of sorption enhancement and adsorbed water (Fig. 12), to those of the FB configuration (Fig. 10). The graphs (c), (f), and (i) show that the breakthrough curve tailed substantially longer in the FB case than in the BFB, which indicates more potential for synthesis-regeneration cycle optimization in a BFB reactor.

In the BFB experiments, the water uptake remained consistent across all temperatures, ranging from 0.11 to 0.12 g of liquid H_2O. A consistent over-stochiometric water adsorption was also observed between 220 and 250 °C, reflecting the reduction in both total amounts of CO and CH_3OH produced as temperature increased. Due to the higher standard conversion measured at 250 °C for CO, the discrepancy between additional amount of reaction products and adsorbed steam reduced at this temperature. Again, water removal with limited adsorption capacity continued after sorption enhancement ended.

Fig. 13 shows a maximum product yield for CH_3OH (a) compared to its equilibrium value between 160 and 163 % across the temperature range of 220–250 °C. For CO (b), the relative enhancement ranged between 166 and 185 %. As for the FB configuration, the error bars in the figure (standard deviation) were derived from a dedicated repeatability test conducted at 250 °C, with absolute standard deviations below 0.01 % for methanol yields and between 0.2 and 0.4 % for CO yields.

Notably, the maximum yield achievable at 220 °C in the BFB reactor was about 20 % higher than that observed in the FB configuration. In fact, the bubbling fluidization led to more uniform temperature distribution throughout the reactor, reducing the presence of hot spots. At 220 °C, this ensured optimal reaction conditions for methanol synthesis, which is highly temperature sensitive. Moreover, the enhanced mixing and movement of sorbent particles in the BFB configuration facilitated continuous exposure of fresh adsorption sites. However, this may have contributed to a shorter enhancement with increasing temperature because of the sharper H_2O breakthrough, further limiting the additional methanol production at 235 °C and 250 °C compared to the fixed bed.

Verification of the particle size ranges after the fluidization experiments revealed the presence of finer particles than those characterized in Section 2.3.3 for both the catalyst and sorbent. This observation prompted an evaluation of the change in particle size distribution (PSD) during several BFB experiments conducted under the same operating conditions. The resulting PSD is shown in Fig. 14, which compares measurements taken before and after a three-cycle experiment performed at 3 bar and 250 °C. For both materials, the post-experiment PSD exhibited a clear shift towards finer particle sizes than those measured at the beginning. Despite this change, mass spectrometry analyses performed over the three consecutive repetitions showed no significant variation in the measured outputs, indicating that the loss of fine particles occurred predominantly at the onset of fluidization and then remained stable during several hours of operation. For the catalyst, approximately 30 % of the initial mass was lost due to entrainment from the disengagement zone, which explains why the post-experiment weight percentages do not sum to 100 % in Fig. 14(b). In contrast, the sorbent experienced only about a 1 % mass loss, indicating a minimal carryover of fine particles out of the reactor. Considering that under 160 μm size, a mixture of catalyst and sorbent was collected in the sieves, each sieve fraction shown in Fig. 14 was carefully transferred into a vial, photographed, and analyzed via image recognition to determine the catalyst and sorbent proportions. The analysis was calibrated such that completely black particles corresponded to 100 % catalyst content, and the resulting PSD for catalyst and sorbent are as depicted in the graphs (a) and (b) of the figure. Detailed explanation of this analysis is provided in the Supporting information.

The observed loss of 15 % of sorbent and 17 % of catalyst to finer particles, compared to the originally measured PSD, highlights the importance of assessing material stability with respect to entrainment and fine-particle separation. This is strongly recommended for an accurate prediction of bubble- and dense-phase dynamics, as well as sorbent capacity retention, in the design of a larger-scale fluidized-entrained bed reactor. For this preliminary proof-of-concept at lab scale, however, the observed PSD change was demonstrated to be non-critical for predicting the adsorption capacity and the consequent enhancement in MeOH and CO production at the reactor outlet.

The more uniform temperature distribution along the BFB reactor was demonstrated by the measurements of the thermocouples positioned at the porous plate and at 2 cm intervals along the catalyst-sorbent bed. Fig. 15 displays this in-situ temperature distribution for both the fixed (a) and fluidized (b) bed configurations for the situation after sorption enhancement. It confirms isothermal operating conditions for the BFB reactor compared to the FB, where noticeable temperature gradients were observed, especially significant during the SE phase (not shown). Specifically, the exothermic CO_2 hydrogenation and water adsorption caused localized hot spots. Above 8 cm height, far from the heat source, the heat wave was dissipated. Conversely, the BFB reactor maintained a stable temperature distribution across the bed height, highlighting the advantage of fluidization in achieving improved heat transfer thanks to enhanced mixing and reduced heat accumulation. The color gradient in Fig. 15 emphasizes these differences, with the FB

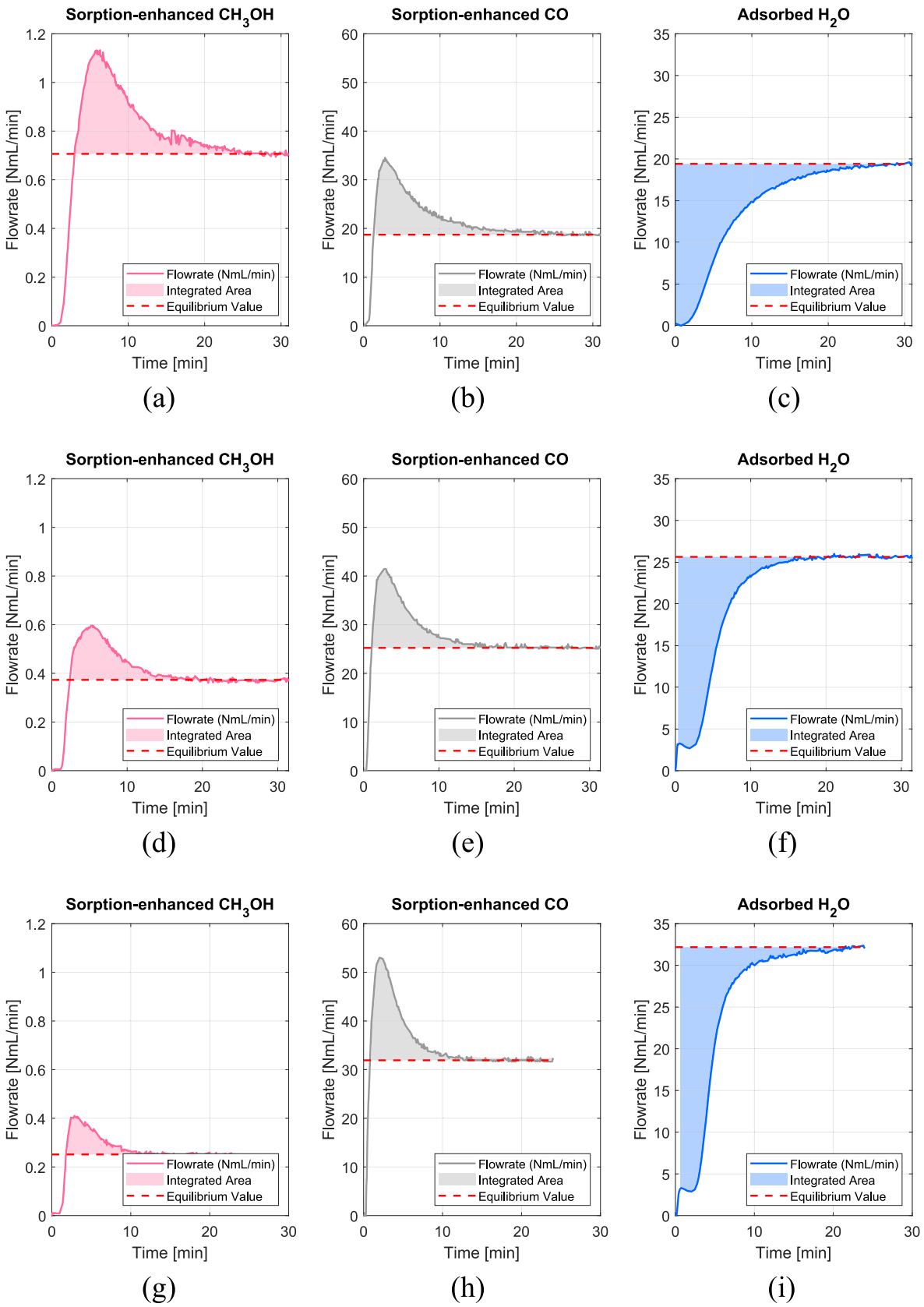

Fig. 12. Visual illustration of the quantified amount of sorption-enhanced CH_3OH and CO produced in comparison to the water uptake (adsorbed H_2O) at the reactor temperature of 220 °C (a) (b) (c), 235 °C (d) (e) (f), and 250 °C (g) (h) (i) for the BFB reactor configuration with 10.9 g CZA and 8.3 g 3 A (inlet composition and pressure as in Table 1). The outlet flow rate evolution over time and integration of the SE area were computed with the MS (CH_3OH and H_2O) and NDIR (CO) data after determining the equilibrium composition.

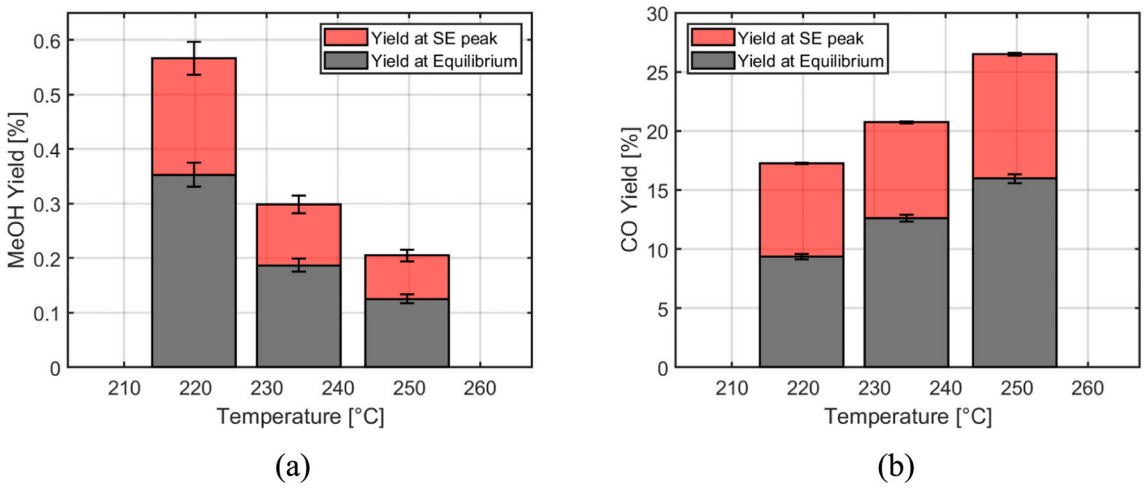

Fig. 13. (a) MeOH yield at the peak of sorption enhancement (red stacked bars) compared to the yield at equilibrium (gray bars) across the investigated temperatures of 220, 235 and 250 °C for a BFB configuration of catalyst-sorbent. (b) Same comparison for CO yield. Error bars (standard deviations) were derived from a repeatability test at 250 °C.

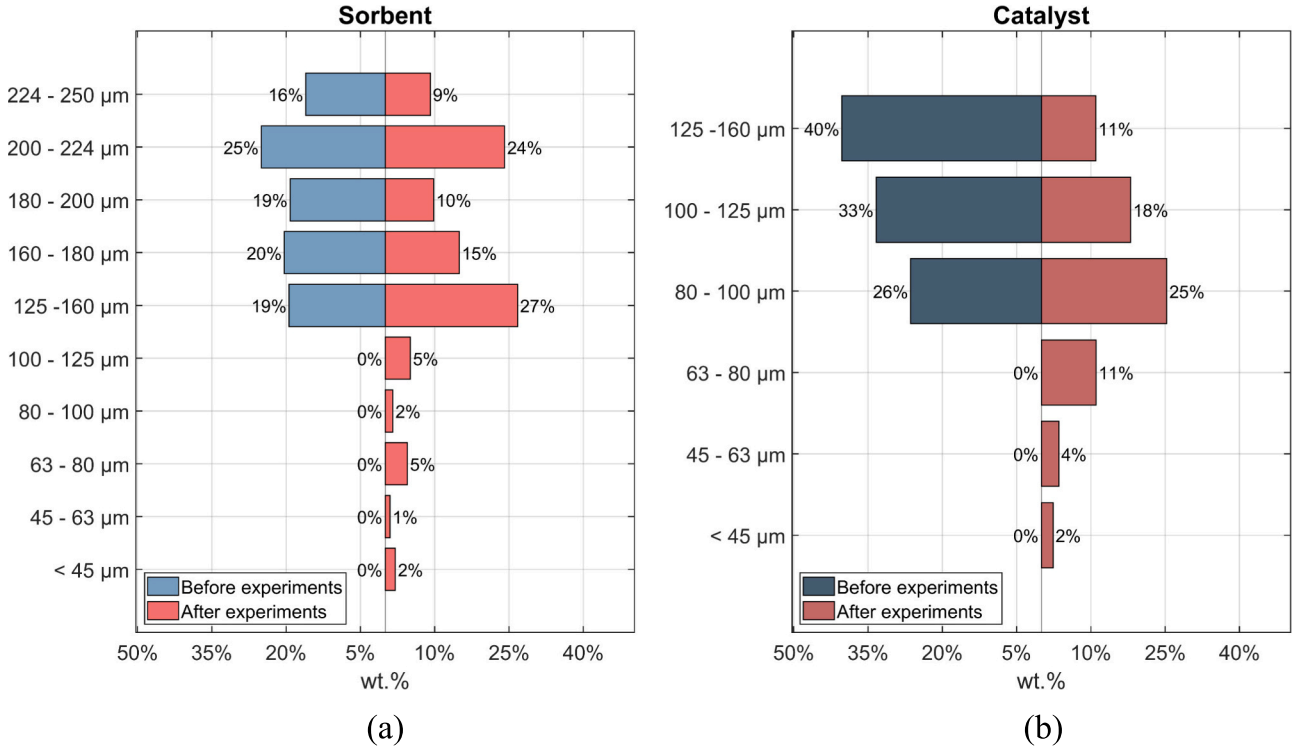

Fig. 14. (a) Particle size distribution (PSD) of the sorbent bed before (bars on the left) and after (bars on the right) performing methanol synthesis at 3 bar and 250 °C in a BFB configuration. (b) Same comparison for the PSD of the catalyst bed. Differences between the total percentages before and after were due to material losses because of entrainment from the reactor.

reactor showing more pronounced shifts (blue to red) compared to the nearly uniform yellow distribution in the BFB temperature profile.

In-situ temperature measurements are necessary to detect localized temperature variations in exothermic processes like FB methanol synthesis, as temperature directly affects the reaction rates, especially during rapid transient phases like sorption enhancement, and equilibrium. Moreover, they ensure accurate characterization of the adsorption process, as the adsorption front moves faster at higher temperatures, anticipating the breakthrough. This is visible in the right plots of Fig. 10, where a plateau in the H_2O signal during adsorption is only visible at 220 °C. For the BFB reactor, the plateau was detected also at 235 °C and 250 °C, although the more effective gas-sorbent contact caused a sharper breakthrough as the adsorption front did not move gradually along the bed. So far, the experimental investigation on sorption-enhanced processes was based on outlet temperature measurements or at the reactor wall [32,54]. However, to rely on these measurements, a sufficient number of thermocouples should be embedded within the setup or reactor structure, complemented by additional equipment for data monitoring [56]. The accuracy of wall and gas temperature measurements provides a basis for representing the heat transfer coefficient in simulation models, enhancing their alignment with the actual process.

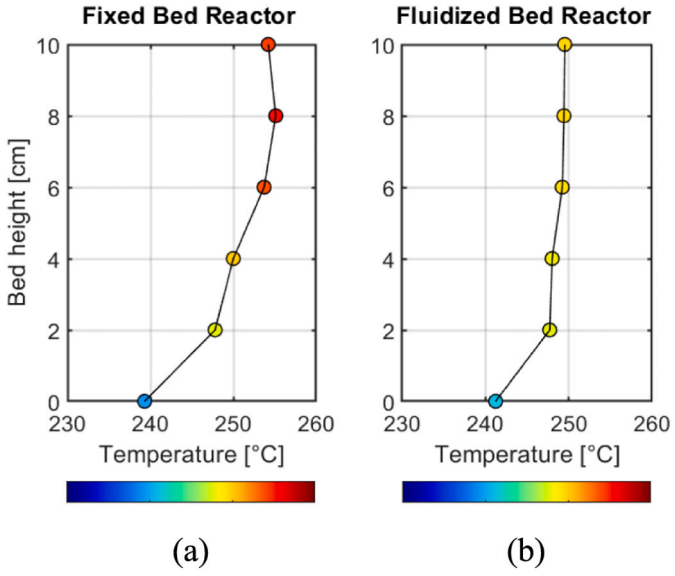

Fig. 15. In-situ temperature profile along the fixed (a) and fluidized bed (b) reactor length from the porous plate to 10 cm bed height. Temperature differences are emphasized with the shift in color set by the color bar.

3.4. *Impact of higher pressures*

Dynamic simulations with the one-dimensional fixed-bed reactor model (cf. to Section 2.4) using the adsorption parameters estimated from the experimental data (Table 2) were used to show the impact of higher pressures. The kinetics are based on Maksimov et al. [32] but were adapted by pre-factors to the experimental results in lab scale to account for the different catalyst used in this work, with focus on the results in the main region of the experimentally investigated domain (around 235 °C). It should be noted that the chosen reactor length and the catalyst hold-up (identical to those used for the lab experiments) allowed to reach steady state, i.e. thermodynamic equilibrium (which in turn was represented in the model by the results of Graaf et al. 2016 [57]). Therefore, the conversion levels and selectivity at steady state are quite independent of the applied kinetic model. The selectivity to be expected during sorption enhancement depends more on the kinetics; therefore, for reactor optimization, a detailed kinetic model of the used commercial catalyst was necessary which, however, is beyond the scope of this paper. Still, the applied modelling approach allowed to derive some fundamental conclusions on useful reactor concepts, the more so as the experimentally determined sorption capacity was used in the model.

As can be observed in Fig. 16, the selectivity towards methanol strongly increases with increasing pressures, both for the steady state situation and the peak during sorption enhancement. Around 10 % methanol yield at steady state and up to 12 % during the enhancement peak were predicted by the chosen modelling approach at 30 bar, the targeted pressure for decentralized applications. The RWGS reaction showed an opposite trend: increasing pressures led to slightly lower CO levels. At 30 bar, a 10 % CO yield was reached during steady state and more than double during the enhancement. The relative contribution of sorption enhancement to the overall methanol yield did not grow linearly with pressure, which can be explained by the Langmuir-type behavior of water adsorption on the sorbents. The water removal does not increase linearly with the partial pressure due to the increasing surface coverage.

The high CO content at the outlet suggests, as already discussed in the experimental section, an intermediate condensation step for methanol removal, followed by a second methanol synthesis reactor that takes advantage of the high CO content, leading to higher methanol yields at equilibrium. To increase the methanol yield during sorption enhancement, significantly more sorbent mass would be necessary due to the limited water uptake per gram of sorbent in HP processes. The already suggested continuous transport of fresh sorbent into the reactor and of spent sorbent to a regenerator would help to avoid expensively

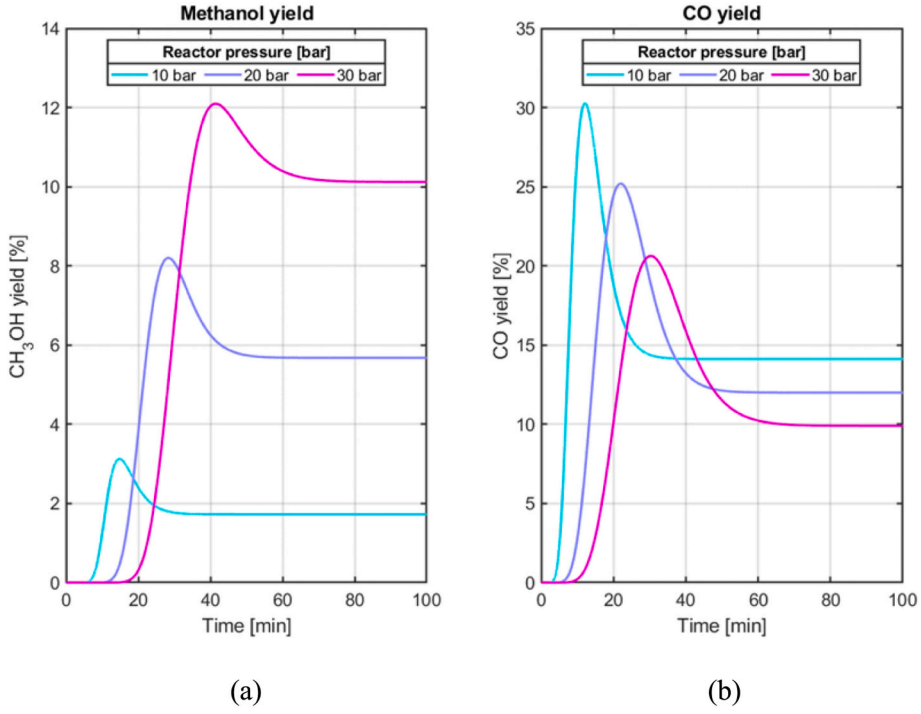

Fig. 16. Influence of increasing pressure on the CH_3OH (a) and CO (b) yields up to the targeted level of 30 bar for process coupling with decentralized green H_2 and biogenic CO_2 supply, as predicted by the one-dimensional fixed-bed reactor model (cf. to section 2.4) using the adsorption parameters estimated from the experimental data (Table 2).

large reactor volumes at high sorbent/catalyst ratios. Moreover, the continuous sorbent transport would allow the reactor to operate close to the peak conditions and the corresponding higher conversion levels, which is favorable for the overall process.

4. Conclusions

This study comprises an extensive experimental investigation aiming at improving product yield beyond its thermodynamic constraints in SE-MeOH synthesis, proving the potential of both fixed and bubbling fluidized bed reactor configurations, with differences in behavior and performance under dynamic conditions. Selective H_2O adsorption and retention of the sorption capacity across a temperature range relevant for MeOH synthesis was evaluated. The sorption-enhancement effect was quantified as a temporary equilibrium shift by computing the water uptake, relative contributions of additional methanol and CO produced during the enhancement phase to the total production, and maximum achievable product yields. A dynamic model for MeOH synthesis in fixed-bed reactors was benchmarked with the lab experiments and used to show the impact of the targeted, industrially relevant pressure range (20–30 bar) for biogenic CO_2 upgrading and green H_2 storage.

It is noted that for both FB and BFB reactor, the sorption enhancement benefited CO formation the most. Although the lab-scale experiments were performed at a lower pressure than industrially applied, the CO enhancement data can guide the design of an adsorptive reactor for LP CO_2-to-syngas production via RWGS, followed by methanol synthesis at higher pressures using reaction (3). As proven by the modelling results, already the targeted pressure level of 20–30 bar (similar to the hydrogen delivery pressure of standard electrolyzers) allows to strongly increase the methanol yield to a range similar to that of the CO yield.

The sorption-enhanced process is inherently time-dependent, with reaction rates declining as the sorbent approaches saturation and the system returns to equilibrium conditions. However, the consistent enhancement observed across the FB and BFB configurations highlights the versatility of the method and the potential for process optimization. This should rely on a more efficient sorbent regeneration strategy with an advanced reactor design, possibly integrating RWGS and MeOH synthesis in sequential stages, making use of CO enhancement.

The BFB configuration offers distinct advantages over the fixed bed, particularly in achieving a more uniform temperature distribution, as confirmed by in-situ measurements, and reducing hot spots caused by exothermic reactions and water adsorption. However, the real potential of a BFB reactor concept lies in facilitating the transport of sorbent particles to a separate regeneration vessel before saturation. Further to improving methanol yield – with its maximum value in this work during fluidized methanol synthesis at 220 °C – this can be achieved with continuous operation by preventing sorbent saturation, thus maintaining methanol production at the sorption-enhancement level.

Thus, an adsorptive BFB reactor could combine sorption enhancement, uninterrupted operation and improved temperature control in compact reactor systems. This approach can address the limitations of traditional methanol synthesis processes, overcoming equilibrium constraints while ensuring optimal reaction conditions with better heat management. These advancements can significantly improve CO_2 utilization coupled with a PtX strategy by storing renewable H_2 in a key molecule for the chemical industry and the energy sector.

Future work should focus on scaling up SE-MeOH synthesis and bridging the gap between lab-scale experiments and industrial applications by means of fluid-dynamic studies and dynamic process simulations with more detailed kinetic models, validated with bench-scale data, for reactor optimization.

CRediT authorship contribution statement

Chiara Berretta: Visualization, Validation, Software, Methodology, Investigation, Funding acquisition, Formal analysis, Data curation, Conceptualization, Writing – original draft. **Mauro Andrea Pappagallo:** Software, Writing – review & editing. **Emanuele Moioli:** Software, Funding acquisition, Writing – review & editing. **Oliver Kröcher:** Resources, Project administration, Writing – review & editing. **Tilman J. Schildhauer:** Validation, Supervision, Resources, Methodology, Funding acquisition, Conceptualization, Writing – review & editing.

Declaration of competing interest

The authors declare no conflict of interest.

Acknowledgments

This project has received funding from the European Union's Horizon 2020 research and innovation programme under the Marie Skłodowska-Curie grant agreement No. 945363, from the Swiss Federal Office of Energy (SFOE) under the project *Efficient Small-Scale methanol synthesis from biogas* (EssMeOH) No. SI/502147, and from the Board of the Swiss Federal Institute of Technology (ETH) under the *Synthetic Fuels from Renewable Resources* initiative. The authors acknowledge the support from the Swiss National Science Foundation (SNSF) Ambizione project: 'Moving catalyst vs. multi-catalyst: determination of the best reactor for the processing of unconventional feedstock' with grant number No. 209125.

The authors would like to thank the following colleagues: Tanja Wieseler (PSI), Julian Indlekofer (PSI), for their support during the experimental campaigns, and Hossein Madi (PSI) for the involvement in outreach activities.

Appendix A. Supplementary data

Supplementary data to this article can be found online at https://doi.org/10.1016/j.cej.2025.170755.

Data availability

Data will be made available on request.

References

[1] A. Goeppert, G.A. Olah, G.K. Surya Prakash, Toward a Sustainable Carbon Cycle, in: Green Chemistry, Elsevier, 2018, pp. 919–962, https://doi.org/10.1016/B978-0-12-809270-5.00031-5.
[2] F. Samimi, M.R. Rahimpour, Direct methanol fuel cell, in: Methanol, Elsevier, 2018, pp. 381–397, https://doi.org/10.1016/B978-0-444-63903-5.00014-5.
[3] X. Zhen, Methanol as an internal combustion on engine fuel, in: Methanol, Elsevier, 2018, pp. 313–337, https://doi.org/10.1016/B978-0-444-63903-5.00011-X.
[4] H. Madi, T. Schildhauer, E. Moioli, Comprehensive analysis of renewable energy integration in decarbonised mobility: leveraging power-to-X storage with biogenic carbon sources, Energ. Conver. Manage. 321 (Dec. 2024) 119081, https://doi.org/10.1016/j.enconman.2024.119081.
[5] V. Eyberg, V. Dieterich, S. Bastek, M. Dossow, H. Spliethoff, S. Fendt, Techno-economic assessment and comparison of Fischer–Tropsch and methanol-to-jet processes to produce sustainable aviation fuel via power-to-liquid, Energ. Conver. Manage. 315 (Sep. 2024) 118728, https://doi.org/10.1016/j.enconman.2024.118728.
[6] G. Bozzano, F. Manenti, Efficient methanol synthesis: perspectives, technologies and optimization strategies, Prog. Energy Combust. Sci. 56 (2016) 71–105, https://doi.org/10.1016/j.pecs.2016.06.001.
[7] G.A. Olah, Beyond oil and gas: the methanol economy, Angew. Chem. Int. Ed. 44 (18) (2005) 2636–2639, https://doi.org/10.1002/anie.200462121.
[8] R.O.D. Santos, L.D.S. Santos, D.M. Prata, Simulation and optimization of a methanol synthesis process from different biogas sources, J. Clean. Prod. 186 (2018) 821–830, https://doi.org/10.1016/j.jclepro.2018.03.108.
[9] H. Arastoopour, The critical contribution of chemical engineering to a pathway to sustainability, Chem. Eng. Sci. 203 (2019) 247–258, https://doi.org/10.1016/j.ces.2019.03.069.
[10] F.M. Baena-Moreno, L. Pastor-Pérez, Q. Wang, T.R. Reina, Bio-methane and bio-methanol co-production from biogas: a profitability analysis to explore new sustainable chemical processes, J. Clean. Prod. 265 (2020) 121909, https://doi.org/10.1016/j.jclepro.2020.121909.
[11] E. Moioli, A. Wötzel, T. Schildhauer, Feasibility assessment of small-scale methanol production via power-to-X, J. Clean. Prod. 359 (2022) 132071, https://doi.org/10.1016/j.jclepro.2022.132071.

[12] A. Sonthalia, N. Kumar, M. Tomar, V. Edwin Geo, S. Thiyagarajan, A. Pugazhendhi, Moving ahead from hydrogen to methanol economy: scope and challenges, Clean Techn. Environ. Policy (2021), https://doi.org/10.1007/s10098-021-02193-x.

[13] M. Bowker, Methanol synthesis from CO_2 hydrogenation, ChemCatChem 11 (17) (2019) 4238–4246, https://doi.org/10.1002/cctc.201900401.

[14] J. Ott, et al., Methanol, in: Ullmann's Encyclopedia of Industrial Chemistry, 1st ed., Wiley-VCH, Ed., Wiley, 2012 https://doi.org/10.1002/14356007.a16_465.pub3.

[15] S. Roy, A. Cherevotan, S.C. Peter, Thermochemical CO2 hydrogenation to single carbon products: scientific and technological challenges, ACS Energy Lett. 3 (8) (2018) 1938–1966, https://doi.org/10.1021/acsenergylett.8b00740.

[16] H.-X. Li, et al., CO2 hydrogenation to methanol over cu/ZnO/Al2O3 catalyst: kinetic modeling based on either single- or dual-active site mechanism, Catal. Lett. 152 (10) (2022) 3110–3124, https://doi.org/10.1007/s10562-021-03913-0.

[17] S. Dang, et al., A review of research progress on heterogeneous catalysts for methanol synthesis from carbon dioxide hydrogenation, Catal. Today 330 (2019) 61–75, https://doi.org/10.1016/j.cattod.2018.04.021.

[18] A.M. Alfantazi, R.R. Moskalyk, Processing of indium: a review, Miner. Eng. 16 (8) (2003) 687–694, https://doi.org/10.1016/s0892-6875(03)00168-7.

[19] E. Moioli, Process intensification and energy transition: a necessary coupling? Chem. Eng. Process. Process Intensif. 179 (2022) 109097 https://doi.org/10.1016/j.cep.2022.109097.

[20] A. Montebelli, C.G. Visconti, G. Groppi, E. Tronconi, C. Ferreira, S. Kohler, Enabling small-scale methanol synthesis reactors through the adoption of highly conductive structured catalysts, Catal. Today 215 (2013) 176–185, https://doi.org/10.1016/j.cattod.2013.02.020.

[21] M.H. Khademi, P. Setoodeh, M.R. Rahimpour, A. Jahanmiri, Optimization of methanol synthesis and cyclohexane dehydrogenation in a thermally coupled reactor using differential evolution (DE) method, Int. J. Hydrog. Energy 34 (16) (2009) 6930–6944, https://doi.org/10.1016/j.ijhydene.2009.06.018.

[22] F. Samimi, S. Kabiri, A. Mirvakili, M.R. Rahimpour, The concept of integrated thermally double coupled reactor for simultaneous production of methanol, hydrogen and gasoline via differential evolution method, J. Nat. Gas Sci. Eng. 14 (2013) 144–157, https://doi.org/10.1016/j.jngse.2013.06.009.

[23] M.R. Rahimpour, F. Rahmani, M. Bayat, E. Pourazadi, Enhancement of simultaneous hydrogen production and methanol synthesis in thermally coupled double-membrane reactor, Int. J. Hydrog. Energy 36 (1) (2011) 284–298, https://doi.org/10.1016/j.ijhydene.2010.09.074.

[24] J. van Kampen, J. Boon, F. van Berkel, J. Vente, M. van Sint Annaland, Steam separation enhanced reactions: review and outlook, Chem. Eng. J. 374 (2019) 1286–1303, https://doi.org/10.1016/j.cej.2019.06.031.

[25] F. Gallucci, Inorganic Membrane Reactors for Methanol Synthesis, in: Methanol, Elsevier, 2018, pp. 493–518, https://doi.org/10.1016/B978-0-444-63903-5.00018-2.

[26] M.J. Bos, D.W.F. Brilman, A novel condensation reactor for efficient CO2 to methanol conversion for storage of renewable electric energy, Chem. Eng. J. 278 (2015) 527–532, https://doi.org/10.1016/j.cej.2014.10.059.

[27] J. Terreni, M. Trottmann, T. Franken, A. Heel, A. Borgschulte, Sorption-enhanced methanol synthesis, Energy Tech. 7 (4) (2019) 1801093, https://doi.org/10.1002/ente.201801093.

[28] H. Nieminen, et al., Process modelling and feasibility study of sorption-enhanced methanol synthesis, Chem. Eng. Process. Process Intensif. 179 (2022) 109052, https://doi.org/10.1016/j.cep.2022.109052.

[29] A. Prašnikar, A. Pavlišič, F. Ruiz-Zepeda, J. Kovač, B. Likozar, Mechanisms of copper-based catalyst deactivation during CO_2 reduction to methanol, Ind. Eng. Chem. Res. 58 (29) (2019) 13021–13029, https://doi.org/10.1021/acs.iecr.9b01898.

[30] J. Van Kampen, J. Boon, M. Van Sint Annaland, Steam adsorption on molecular sieve 3A for sorption enhanced reaction processes, Adsorption 27 (4) (2021) 577–589, https://doi.org/10.1007/s10450-020-00283-8.

[31] K. Wein, T. Kunz, J. Friedland, R. Güttel, Kinetic effect of in situ water adsorption during CO2 hydrogenation: an experimental investigation, Chem. Eng. Sci. 285 (2024) 119537, https://doi.org/10.1016/j.ces.2023.119537.

[32] P. Maksimov, A. Laari, V. Ruuskanen, T. Koiranen, J. Ahola, Methanol synthesis through sorption enhanced carbon dioxide hydrogenation, Chem. Eng. J. 418 (2021) 129290, https://doi.org/10.1016/j.cej.2021.129290.

[33] P. Maksimov, H. Nieminen, A. Laari, T. Koiranen, Sorption enhanced carbon dioxide hydrogenation to methanol: process design and optimization, Chem. Eng. Sci. 252 (2022) 117498, https://doi.org/10.1016/j.ces.2022.117498.

[34] E. Moioli, T. Schildhauer, Tailoring the reactor properties in the small-scale sorption-enhanced methanol synthesis, Chem. Ing. Tech. 95 (5) (2023) 631–641, https://doi.org/10.1002/cite.202200200.

[35] F. Massa, F. Scala, A. Coppola, Simulation of biogas upgrading by sorption-enhanced methanation with CaO in a dual interconnected fluidized bed system, Processes 11 (11) (2023) 3218, https://doi.org/10.3390/pr11113218.

[36] E. Moioli, T. Schildhauer, A system for the combined carbon capture and utilization to produce renewable methanol from biogas, Chem. Ing. Tech. (2024) 826–839, https://doi.org/10.1002/cite.202300200.

[37] M. Bayat, M. Heravi, M.R. Rahimpour, Sorption enhanced process by integrated heat-exchanger reactor assisted by fluidization concept for methanol synthesis, Chem. Eng. Process. Process Intensif. 110 (2016) 30–43, https://doi.org/10.1016/j.cep.2016.09.018.

[38] S. Walspurger, G.D. Elzinga, J.W. Dijkstra, M. Sarić, W.G. Haije, Sorption enhanced methanation for substitute natural gas production: experimental results and thermodynamic considerations, Chem. Eng. J. 242 (2014) 379–386, https://doi.org/10.1016/j.cej.2013.12.045.

[39] J. Boon, P.D. Cobden, H.A.J. Van Dijk, C. Hoogland, E.R. Van Selow, M. Van Sint Annaland, Isotherm model for high-temperature, high-pressure adsorption of and on K-promoted hydrotalcite, Chem. Eng. J. 248 (2014) 406–414, https://doi.org/10.1016/j.cej.2014.03.056.

[40] C. Unluer, A. Al-Tabbaa, Characterization of light and heavy hydrated magnesium carbonates using thermal analysis, J. Therm. Anal. Calorim. 115 (1) (2014) 595–607, https://doi.org/10.1007/s10973-013-3300-3.

[41] MASsoft-V7-Training-Manual.pdf, Accessed: Dec. 05, Online]. Available, https://www.hideninc.com/tech/MASsoft-V7-Training-Manual.pdf, 2024.

[42] A. Beck, M.A. Newton, M. Zabilskiy, P. Rzepka, M.G. Willinger, J.A. van Bokhoven, Drastic events and gradual change define the structure of an active copper-zinc-alumina catalyst for methanol synthesis, Angew. Chem. Int. Ed. 61 (15) (2022) e202200301, https://doi.org/10.1002/anie.202200301.

[43] P.F. Riechmann, "Cross verified independent measurements of correlated bubble property distributions as part of the scale-up of a catalytic bubbling fluidized bed reactor," EPFL, Lausanne (2022), https://doi.org/10.5075/epfl-thesis-9873.

[44] A. R. Abrahamsen. Geldart, "Behaviour of Gas-Fluidized Beds of Fine Powders Part II. Voidage of the Dense Phas in Bubbling Beds" (n.d.).

[45] L. Pompilio, D. DePaoli, B. Spencer, Evaluation of INL supplied MOOSE/OSPREY model: modeling water adsorption on type 3A molecular sieve, ORNL/LTR-2014/340 1160338 (2014), https://doi.org/10.2172/1160338.

[46] J.A.D. Dobladez, V.I.Á. Maté, S.Á. Torrellas, M. Larriba, G. Pascual Muñoz, R. Alberola Sánchez, Comparative simulation study of methanol production by CO2 hydrogenation with 3A, 4A and 5A zeolites as adsorbents in a PSA reactor, Sep. Purif. Technol. 262 (2021) 118292, https://doi.org/10.1016/j.seppur.2020.118292.

[47] G.H. Graaf, E.J. Stamhuis, A.A.C.M. Beenackers, Kinetics of low-pressure methanol synthesis, Chem. Eng. Sci. 43 (12) (1988) 3185–3195, https://doi.org/10.1016/0009-2509(88)85127-3.

[48] S. Sircar and A. L. Myers, "Gas Separation by Zeolites" (n.d.).

[49] J.M. Crawford, et al., High selectivity reactive carbon dioxide capture over zeolite dual-functional materials, ACS Catal. 14 (11) (2024) 8541–8548, https://doi.org/10.1021/acscatal.4c01340.

[50] A. Ferre, J. Burger, Coadsorption equilibria on molecular sieves 3A and densities of liquid mixtures containing formaldehyde, methanol, and water at 295.15 and 313.15 K, Ind. Eng. Chem. Res. 60 (42) (2021) 15256–15263, https://doi.org/10.1021/acs.iecr.1c02778.

[51] B. Peng, H. Dou, H. Shi, E.E. Ember, J.A. Lercher, Overcoming thermodynamic limitations in dimethyl carbonate synthesis from methanol and CO2, Catal. Lett. 148 (7) (2018) 1914–1919, https://doi.org/10.1007/s10562-018-2402-8.

[52] Y. Cul, et al., Latest catalyst provides more methanol for longer, 2021.

[53] G.J. Fulham, X. Wu, W. Liu, E.J. Marek, Mechanistic insights into the role of zinc oxide, zirconia and ceria supports in cu-based catalysts for CO2 hydrogenation to methanol, Chem. Eng. J. 480 (2024) 147732, https://doi.org/10.1016/j.cej.2023.147732.

[54] A. Borgschulte, et al., Sorption enhanced CO2 methanation, Phys. Chem. Chem. Phys. 15 (24) (2013) 9620, https://doi.org/10.1039/c3cp51408k.

[55] A. Borgschulte, et al., Manipulating the reaction path of the CO_2 hydrogenation reaction in molecular sieves, Cat. Sci. Technol. 5 (9) (2015) 4613–4621, https://doi.org/10.1039/C5CY00528K.

[56] D.S. Martínez, F. Illán, J.P. Solano, A. Viedma, Embedded thermocouple wall temperature measurement technique for scraped surface heat exchangers, Appl. Therm. Eng. 114 (2017) 793–801, https://doi.org/10.1016/j.applthermaleng.2016.12.039.

[57] G.H. Graaf, J.G.M. Winkelman, Chemical equilibria in methanol synthesis including the water–gas shift reaction: a critical reassessment, Ind. Eng. Chem. Res. 55 (20) (2016) 5854–5864, https://doi.org/10.1021/acs.iecr.6b00815.